MITIGATION OF INTERFERENCE FROM IRIDIUM SATELLITES BY PARAMETRIC ESTIMATION AND SUBTRACTION

Chowdhury M.R. Shahriar

THESIS SUBMITTED TO THE FACULTY OF
VIRGINIA POLYTECHNIC INSTITUTE AND STATE UNIVERSITY
IN PARTIAL FULFILLMENT OF THE
REQUIREMENTS FOR THE DEGREE OF

MASTER OF SCIENCE
IN
ELECTRICAL ENGINEERING

STEVEN W. ELLINGSON, CHAIR
MICHAEL BUEHRER, MEMBER
JEFFREY REED, MEMBER

DECEMBER 01, 2006
BLACKSBURG, VIRGINIA 24061

KEYWORDS: SATELLITE, COMMUNICATIONS, DSP, PARAMETRIC ESTIMATION,
RADIO ASTRONOMY, RADIOMETRY, L-BAND, DETECTION

Mitigation of Interference From Iridium Satellites By Parametric Estimation And Subtraction

Chowdhury M.R. Shahriar

ABSTRACT

Radio astronomy is the science of observing the universe at radio frequencies. In recent years, radio astronomy has faced a growing interference problem as radio frequency (RF) bandwidth has become an increasingly scarce commodity. Communication systems such as Earth orbiting communication satellites creates severe interference to the radio telescopes. This thesis proposes an algorithm to mitigate the radio frequency interference (RFI) from the Iridium satellite system. A technique is presented here to detect the downlink signal of Iridium, estimate the parameters of the signal, synthesize the noise-free version of the signal and finally subtract the recreated signal from the radio telescope output. Using both simulated and real data captured by a radio telescope testbed, we demonstrate that for Iridium bursts with 20 dB signal to noise power ratio (SNR), the proposed algorithm achieves more than 15 dB cancellation. The method proposed here can be implemented using present-day digital signal processing hardware and software. A performance analysis of this proposed cancellation scheme in the radio astronomy RFI mitigation regime is presented.

Acknowledgements

I would like to express my gratitude to Dr. Steven Ellingson for his constant encouragement and belief in me. He has been everything that one could want in an advisor. I am deeply indebted to my committee members Dr. Jeffrey H. Reed, and Dr. Buhrer for providing valuable advice. I also want to thank Patrick McDougle for sharing his expertise of Argus Antenna System. I thank the wonderful staff of MPRG for their assistance. Finally, most of all, I thank my wife and my parents for their unconditional love and support.

Blacksburg, Virginia — Chowdhury Shahriar
May 01, 2006

To my mother Suraiya Begum, father Rafiqul I. Chowdhury, sister Sonia Sonahi Chowdhury, wife Mahin Khan, grandfather Shafiuddin Ahmed, grandmother Latifa Begum, uncle Mizanur Rahman, Mostafizur Rahman, Mahbubur Rahman, Mushfiqur Rahman, aunty Sultana Parvin, my mentor Matiur Rahman, Zainul Abedin and my friend Russel, Baki, Manju, Shanto, Tapu, Niaz, Tanvir, Salim, Dale, Amit, Rahat, Kamol, Tuhin, Dr. Fakhrul Alam, Dr. Rushad Faridi, Nighat Jahan Suzana, Mostafa Naquib Ahsan, and Bashirul A. Polash, without their support, laughter, and dedication, none of my achievements would have been possible.

Table of Contents

List of Figures

List of Tables

Chapter 1

Introduction

1.1 Introduction

Radio astronomy has been a major factor in revolutionizing our concepts of the universe and how it works. Radio astronomy is the study of distant objects in the universe by collecting and analyzing the radio waves emitted by those objects. Typical radio astronomy signals are weaker than the signals used in terrestrial communication systems. Relatively strong signals from different communication devices can cause severe interference to these weaker radio signals. As use of radio for devices such as cellular telephones, wireless computer networks, and a whole host of other uses continues to increase, the threats to radio astronomy from communication transmitters increases.

A prime threat comes from transmitters in orbiting Earth satellites, since those transmitters are located overhead, precisely where radio astronomers must aim their telescopes to study the universe. For example, the downlink signal from Iridium interferes with the radio telescopes. The scope of this thesis is to mitigate the interference caused by the downlink signal of Iridium. An algorithm is presented here to detect the signal from Iridium, estimate the signal, recreate it using estimated parameters and finally subtract it from the radio telescope. The key challenge of this thesis is to

estimate the unknown parameters of of the received signal.

1.2 Thesis Outline

The remainder of this thesis is organized as follows:

Chapter 2, *The Iridium Problem in L-Band Radiometry*, presents a brief overview of current L-band radiometry and radio frequency interference (RFI). This chapter describes Iridium satellite system and its role as an interferer to L-band radiometry. It also includes a brief literature survey on RFI mitigation techniques applicable to Iridium.

Chapter 3, *Technical Specification of Iridium*, presents the detailed technical specification of the Iridium satellite system. This chapter describes Iridium's orbital characteristics and constellation, transmission band, and downlink signal properties.

Chapter 4, *Algorithm*, presents the proposed algorithm. This chapter describes data model for Iridium downlink signal, high level block diagram of the proposed algorithm, and detailed description of the proposed algorithm. This chapter also includes the details of algorithm implementation.

Chapter 5, *Algorithm Validation by Simulation*, presents simulation methodology, Iridium burst detection performance, RFI cancelation performance, and performance of the complete proposed algorithm. This chapter also includes a comparison between the proposed algorithm and simpler technique based on blanking.

Chapter 6, *Algorithm Validation by Real Data*, presents details about the radio telescope used to capture the real data, characteristics of real dataset, and a comparison of algorithm performed for real dataset.

Chapter 7, *Conclusion*, summerizes this thesis' contributions along with suggestions possible future research.

Appendix A, *Copyright Permission*, contains the formal permission letter of the copyrighted images used in this thesis.

1.3 Research Summary

The thesis describes a technique to mitigate radio frequency interference (RFI) from Iridium. In this thesis, an algorithm to "detect/cancel" the RFI from Iridium is presented. An algorithm was proposed to mitigate RFI from Iridium. The proposed algorithm was a temporal method in which Iridium signal was detected, estimated, synthesized, and finally subtracted from the telescope input. Proposed algorithm was validated using simulated Iridium data. A complete performance of the system was simulated and analyzed for simulated data. Proposed algorithm was also validated using real data captured from the Argus radio telescope to verify the effectiveness of proposed algorithm in a real world scenario. A comparative study between the performances of the proposed algorithm (detect/cancel) with another well known algorithm (detect/blank) was conducted for both simulated and real data.

Chapter 2

The Iridium Problem in L-Band Radiometry

In this chapter, a brief overview of L-band radiometry and Iridium's impact as an interferer in is presented. In Section 2.1, a brief description of L-band radiometry and radio frequency interference (RFI) is presented. The Iridium satellite system is described Section 2.2. Section 2.3 has a brief literature survey on different methods of mitigating RFI caused by Iridium.

2.1 L-Band Radiometry and RFI

Radiometry is the measurement of radio frequency intensity. Radio astronomy is the science of observing the universe using radiometry. In recent years, radio astronomy has faced a growing interference problem as competition for radio frequency (RF) spectrum has emerged from commercial communications. The radio signals arriving at Earth from astronomical objects are extremely weak. They are many orders of magnitude weaker than the signals used by communication systems. Because the cosmic radio sources are so weak, they are easily masked by man-made interference.

By international agreement, radio frequencies are divided up into blocks, or bands,

designated for different types of uses. A number of frequency bands are allocated exclusively to radio astronomy. Because radio astronomers do their work with extremely sensitive receiving equipment, transmitting in these bands is generally prohibited. However, transmitters using frequencies near those assigned to radio astronomy can nevertheless cause interference to radio telescopes. This occurs when the transmitter's output is excessively "broad" with sidelobes spilling over into the radio astronomy frequencies, or when the transmitter emits spurious signals outside its designated frequency range. Also, operating outside the protected bands is often desirable for scientific reasons; resulting in the situation that the RFI center frequency might overlap astronomy.

One particular frequency range that is severely affected is known as L-band. Various definitions of "L-Band" exist, but for the purpose of this work we consider it to include the 1.0-1.7 GHz band [2]. L-band is heavily used in radio astronomical research. For example, $1215 - 1420.41$ MHz band is used for spectroscopy of neutral hydrogen at high redshift, pulsar observation, and the search for extra-terrestrial intelligence (SETI). The 1612 MHz spectral line emission of hydroxyl (OH) is used to explore the properties of evolved stars and the galactic dynamics [3]; the $1610.6 - 1613.8$ MHz of L-band is allocated to the radio astronomy service (RAS) on a primary basis by International Telecommunications Union (ITU) [4].

L-band is also used for both satellite communications and terrestrial communications. ITU allocated $1610.6 - 1626.5$ MHz of L-band to the mobile-satellite service, MSS (Earth-to-space) on a primary basis, and MSS (space-to-Earth) has a secondary status in the band $1613.8 - 1626.5$ MHz. $1610.6 - 1626.5$ MHz of L-band is also used for aeronautical radio navigation [4]. All these communications transmission create

interference to L-Band radio astronomy. For example, a major source of interference is the downlink transmission from Iridium satellites. Transmissions from Iridium satellites cause particular disruption to searches for OH megamasers because their signals are nearly always present, and because they cover a wide range of frequencies [3]. RFI caused by the Iridium and the method of mitigating RFI from Iridium are the key topics of this thesis.

2.2 Iridium Satellite System and Effect on L-Band Radiometry

The Iridium satellite system is a provider of global, mobile satellite voice and data solutions with complete coverage of the Earth (including oceans, airways and polar regions). Through a constellation of 66 low Earth orbiting (LEO) satellites, Iridium delivers communications services to and from remote areas where other forms of communications are either unavailable or unreliable [5]. The concept of the Iridium satellite system was first proposed by the famous communications company Motorola Inc. in the early 1990's. The rationale for Iridium was to build a single united platform for both mobile users and fixed sites all over the world which would provide seamless voice and data communications. The initial proposal included 77 active satellites constellation in seven orbital planes, and was named after the element iridium, which has atomic number 77. Later Motorola modified their plan and decided to have 66 satellites in six orbital planes [6].

On January 31, 1995 the FCC granted licenses to Iridium. Immediately thereafter, Iridium began commercial testing with a limited number of customers who did not have to pay for the service. Full commercial service began in November 1, 1998

[6]. Call quality received mixed reports in the early months, and service growth was slowed by delays in both production and distribution of subscriber phones. Even though Iridium is considered to be a technological marvel, it faced financial crisis due to insufficient demand for the service. As a result Iridium went into Chapter 11 bankruptcy on August 13, 1999 [7]. Nowadays the system is being used primarily by the U.S. Department of Defense (DoD). Iridium also serves civilians through a commercial gateway in Tempe, Arizona. Iridium Satellite LLC claims to have approximately $137,500$ subscribers as of September 30, 2005 [5].

The Iridium satellite system caused a lot of trouble for the radio astronomy service since it's beginning. For example, the downlink (space-to-Earth) signals from Iridium span the range $1621.35 - 1626.5$ MHz and are quite strong. The important OH transition at 1612.231 MHz lies very close to the Iridium downlink signal, and significant sideband emission from Iridium can sometimes be seen as low as 1619 MHz [8]. Furthermore, it is found by radio astronomical observations that the Iridium downlink transmissions in the band $1621.35 - 1626.5$ MHz cause harmful interference of up to 30 dB above the levels deemed harmful as given in ITU-R Recommendation RA.769 [4]. Motorola stated that the downlink transmissions could meet the Recommendation ITU-R RA769 levels for harmful interference only during periods of low traffic [9]. In practice, this interference could meet the Recommendation ITU-R RA769 level for about 4 hours per day (night hours), which is problematic for many radio astronomical projects, especially for those where daytime observations are required on scientific grounds [10].

Motorola proposed some possible solutions to radio astronomy stations [3]. However, these would affect radio astronomy observations only without having any impact

on Iridium system's operations. For example, recently Iridium LLC suggested that radio astronomy observations should be scheduled avoiding peak traffic periods of the Iridium. Such a method might be helpful to avoid interference from Iridium temporarily, though the problem is yet far from being a satisfactory long term solution.

2.3 Literature Survey on Mitigation of Iridium RFI in L-Band

The problem of how to suppress RFI from Iridium in radio astronomy has received some attention. One prominent method for real time mitigation is time domain blanking [11] [12]. In this method, the data corrupted by interfering bursts is zeroed out. This consists of a two step process: (1) burst detection and (2) blanking of the burst interval. The burst detection threshold and the blanking interval must be chosen to effectively implement time blanking. The burst detection threshold is the level above the average noise power that an RFI burst must be to declare the presence of a burst. The blanking interval is the duration that is blanked when a burst is detected. Since "zeroing" the data completely removes the RFI, the primary limitation of blanking is detection performance [11]. It is inevitable that some fraction of weak but potentially damaging pulses will not be detected, and thus will not be blanked.

Another type of RFI mitigation relevant to Iridium is temporal cancellation. In this method, advance knowledge of the RFI waveform is exploited to coherently subtract the interfering pulse [11] [13]. In [11], this method is used to mitigate radar interference in L-band radio astronomy; it is assumed that the propagation channel can be modeled as a complex-valued constant α over the period of single radar pulse.

One can estimate α simply by comparing the measured magnitude and the phase with that of a model transmitted pulse. If the received signal is $x(t)$, known signal is $p(t)_j$ and the estimated complex value is $\hat{\alpha}$, then RFI can be removed by subtracting $\hat{\alpha}p(t)$ from $x(t)$. Temporal canceling involves a significant risk that the waveform is not properly estimated, and therefore not completely removed when the synthesized waveform is subtracted [14] [12]. The goal of the work presented in this thesis is to apply this technique to Iridium. Additional real time techniques applicable to Iridium exist, including for example spatial nulling [15].

Chapter 3

Technical Description of Iridium

In this chapter, a brief technical description of the Iridium satellite system is presented. In Section 3.1, a brief overview of the Iridium system is presented. In Section 3.2, a description of Iridium transmission bands is presented. In Section 3.3, a description of Iridium channel multiplexing and frame structure is presented. Section 3.4 includes details about relevant L-band transmission characteristics.

3.1 Iridium Satellite System Overview

The Iridium satellite system has three segments: (1) satellites, (2) subscriber terminals and (3) terrestrial base-stations. There are total of 66 active low-earth orbiting (LEO) satellites in Iridium constellations orbiting at a height of approximately 485 miles [5]. They circle the earth once every 100 minutes 28 seconds traveling at a rate of 16,832 miles per hour [5]. There are total 6 orbital planes for the satellites and the average inclination of the orbital planes is 86.4 degrees. Each satellite weights about 1500 pounds. Figure 3.1 and shows the constellation of Iridium satellite system.

Each Iridium satellite has a 1400 W transmitter and maintains 16 dB link margin [16]. Each satellite communicates with subscriber equipment using "main mission"

antennas. Each satellite has three main mission L-band phased array antennas. Each of the satellites can produce 48 spot beams [6]. Figure 3.2 shows the footprint of current Iridium satellite system at a moment in time. Apart from the three main mission antennas, there are four crosslink antennas in each satellite. The crosslink antennas permit satellites in the constellation to send traffic from one Iridium satellite to another. Table 3.1 has the technical specification of the Iridium satellite transmitter.

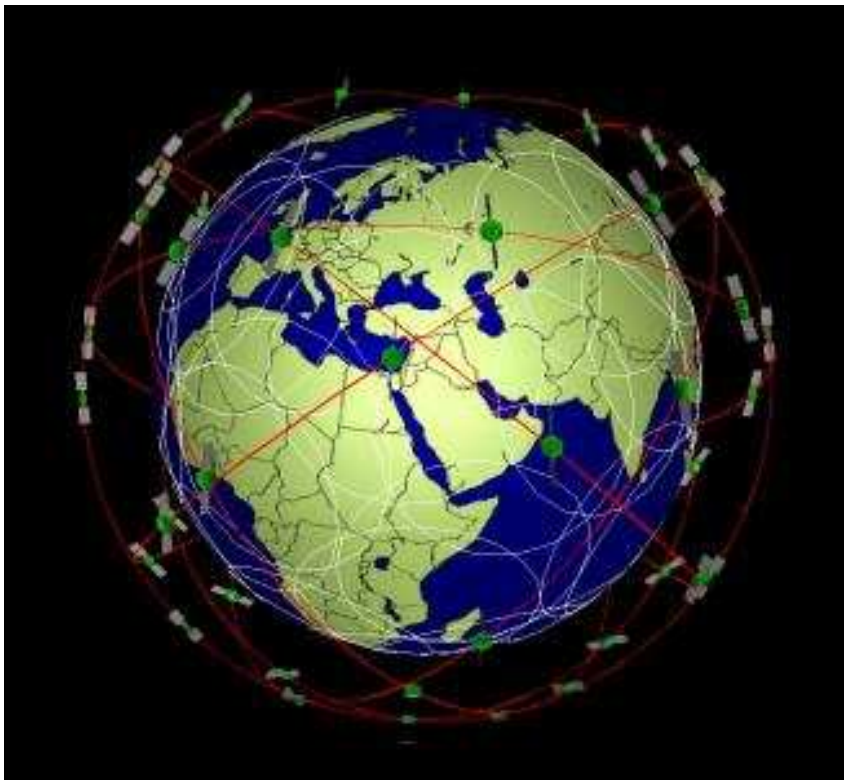

Figure 3.1: Iridium satellite constellation [1]

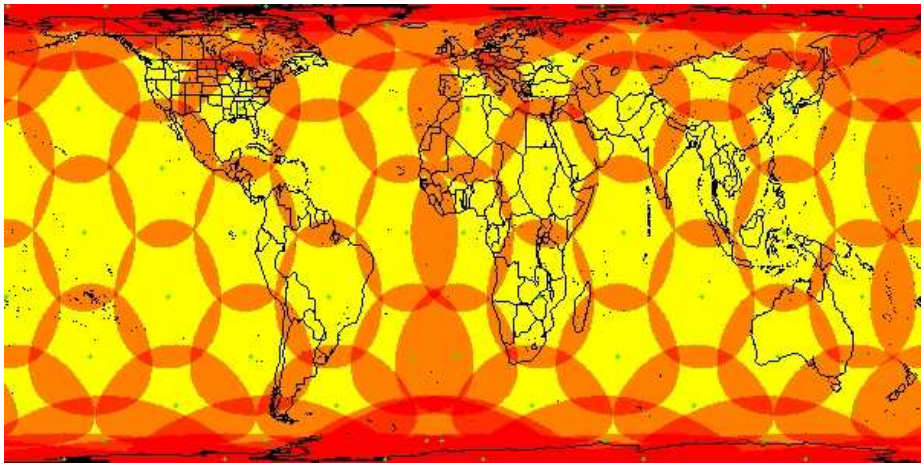

Figure 3.2: Spot beam footprint of current Iridium satellite system [1]

Table 3.1: Iridium specifications

Parameter	*Specification*
Number of Satellites	66
Number of Orbital Planes	6
Approx. distance from Earth	780 km
Period	100.1 minutes
Polarization	right hand circular
Average EIRP	-13.0 dBW/4kHz
Antenna Gain	24.3 dBi/cell
Transmitter Power	1400 W
Beam Width	30 miles diameter
Bandwidth	10.5 MHz, 41.67 kHz per channel
Number of Channels	240 (20 per cell) (full band)
Band Center Frequency	$1616 + 0.021875(2n - 1)$ MHz where (n = 1, ..., 240)

3.2 Iridium Transmission Network

The Iridium transmission network consists of two-way communication links between satellites and end users (subscribers), satellites to base-stations, and satellites to satellites. Each end-user can directly send and receive signal from satellites. Each satellite has direct two-way communication with base stations (both control centers and gateways). With four crosslink antennas, each satellite is cross-linked to four other satellites. These cross-linked satellites operate as a fully meshed network. Note that, in the full mesh network topology, each node (satellite or other device) is connected directly to several others. This inter-satellite networking is a significant feature of Iridium system as this allows two-way communication between satellites, base stations, and subscriber units. Figure 3.3 shows the Iridium communication network.

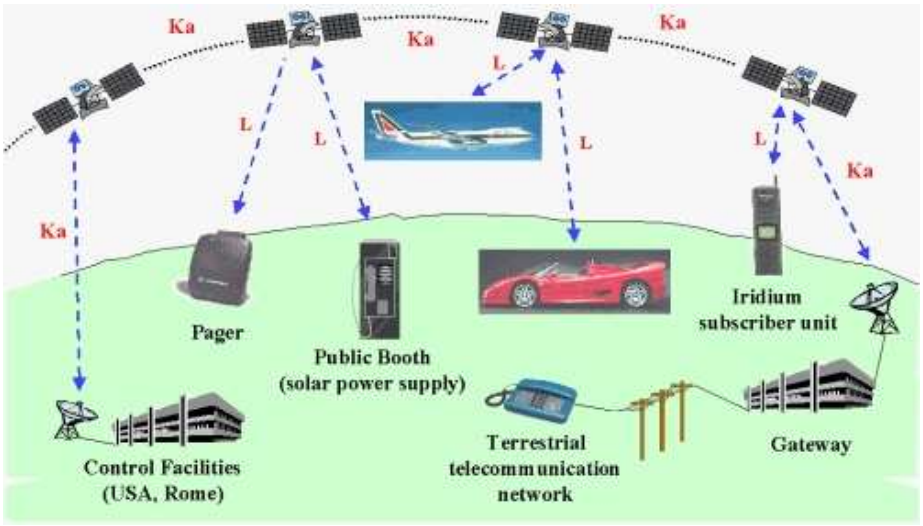

Figure 3.3: Iridium satellite communication network [1]

Table 3.2: Iridium frequency plan

Band	*Frequency Range*	*Link*	*Purpose*
L	1610.00 to 1626.50 MHz	Mobile to satellite (Uplink)	System frequencies
L	1621.35 to 1626.50 MHz	Mobile to satellite (Uplink)	Licensed frequencies
L	1610.00 to 1626.50 MHz	Satellite to mobile (Downlink)	System frequencies
L	1621.35 to 1626.50 MHz	Satellite to mobile (Downlink)	Licensed frequencies

The Iridium system uses various bands for transmitting signals. For example, Ka-band links between satellites and base-stations, L-band links between satellites and end users, and Ka-band cross links between satellites [6]. In Table 3.2, Iridium downlink signal transmission band, frequency, and use is given.

3.3 Iridium Channel Multiplexing and Frame Characteristics

Iridium system uses a hybrid time division multiple access/frequency division multiple access (TDMA/FDMA) architecture based on Time Division Duplex (TDD) using a 90 ms frame [6]. In a TDD system a common carrier is shared between the uplink and downlink, the resource being switched in time. Users are allocated one or more timeslots for uplink and downlink transmission. The main advantage of TDD operation is that it allows asymmetric flow which is more suited to data transmission.

3.3.1 TDMA Frame

The basic unit of the TDMA channel is a time slot. Time slots are organized into frames. The frame consists of a 20.32 ms downlink simplex time slot, followed by four 8.2 ms uplink time slots and four downlink time slots, which provide the duplex channel capability [6]. The TDMA frame also includes various guard times to allow

hardware set up and to provide tolerance for uplink channel operations. The L-band subsystem TDMA frame is illustrated in Figure 3.4.

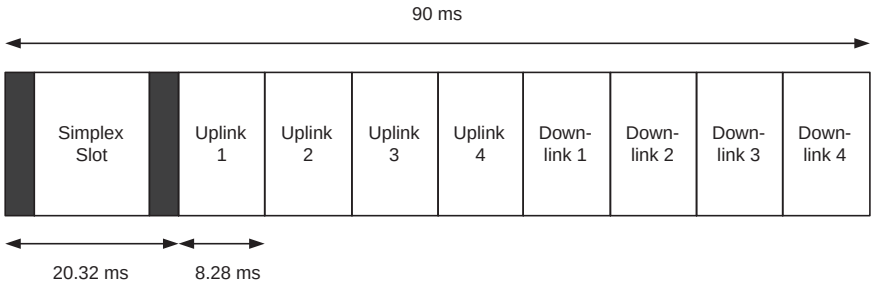

Figure 3.4: TDMA frame structure

The simplex timeslot supports the downlink only, ring, and messaging channels. The Acquisition, Synchronization, and Traffic channels use the uplink timeslots. The Broadcast, Synchronization, and Traffic channels use the downlink duplex timeslots. The L-band frame provides 2250 symbols per frame at 25 kSy/s. A 2400 bps traffic channel uses one uplink and one downlink time-slot each frame [6].

3.3.2 FDMA Frequency Plan

The basic unit of frequency in the FDMA structure is a frequency access that occupies a 41.667 kHz bandwidth [6]. Each channel uses one frequency access. The frequency accesses are divided into the duplex channel band and the simplex channel band.

Duplex Channel Band

The frequency accesses used for duplex channels are organized into sub-bands, each of which contains eight frequency accesses. Each sub-band, therefore, occupies 333.333 kHz (8×41.667 kHz.) In duplex operation, the Iridium system is capable

of operating with up to 30 sub-bands that is, in regions with 10.5 MHz licenses, containing a total of 240 frequency accesses [6].

Simplex Channel Band

A 12-frequency access band is reserved for the simplex (ring alert and messaging) channels. These channels are located in a globally allocated 500 kHz band between 1626.0 MHz and 1626.5 MHz [6]. These frequency accesses are only used for downlink signals and they are the only L-band frequencies that may be transmitted during the simplex time-slot.

3.4 L-Band Downlink Transmission Characteristics

Iridium downlink signals are transmitted as a burst. Each burst has three segments: (1) preamble, (2) unique word, and (3) data. A description of each of this segments are presented below. Figure 3.5 shows a block diagram of the downlink signal burst generation technique and Figure 3.6 shows the structure of downlink burst.

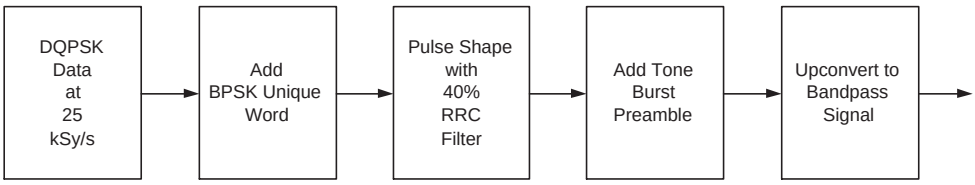

Figure 3.5: Downlink signal generation technique

At the beginning, data bits are modulated. All downlink transmission from satellites use DQPSK modulation for information. The modulation structure used for

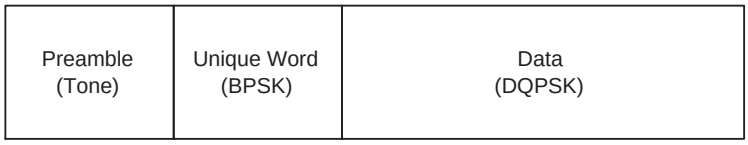

Figure 3.6: Downlink burst structure

downlink traffic data includes differential encoding to allow demodulators to rapidly reacquire phase and to resolve phase ambiguities in case there is a loss of phase-lock due to a link fade. The symbol rate of 25 kSy/s supports a data rate of 50 kbps.

A BPSK modulated unique word is attached at the beginning of the data which enables the receiver to detect the phase rotation introduced by the channel. Both the BPSK modulated unique word and DQPSK modulated data are pulse shaped using a root raised cosine (RRC) filter with rolloff factor of 0.4. A 2.6 ms long tone burst is followed by this unique word and data. The symbols are then up-converted to make it a bandpass signal and transmitted. Figure 3.7 and Figure 3.8 respectively show the Iridium signal waveform magnitude and phase measured by Argus, an instrument described in Chapter 6.

In the downlink burst, the supported vocoder information bit rate is 2.4 kbps for digital voice, fax, and data. With rate 3/4 forward error correction (FEC) coding this becomes 3.45 kbps, which includes overhead and source encoding, exclusive of FEC coding, for weighting of parameters in importance of decoding the signal. The bit error ratio (BER) at threshold is nominally 0.01 but is much better 99 percent of the time [6].

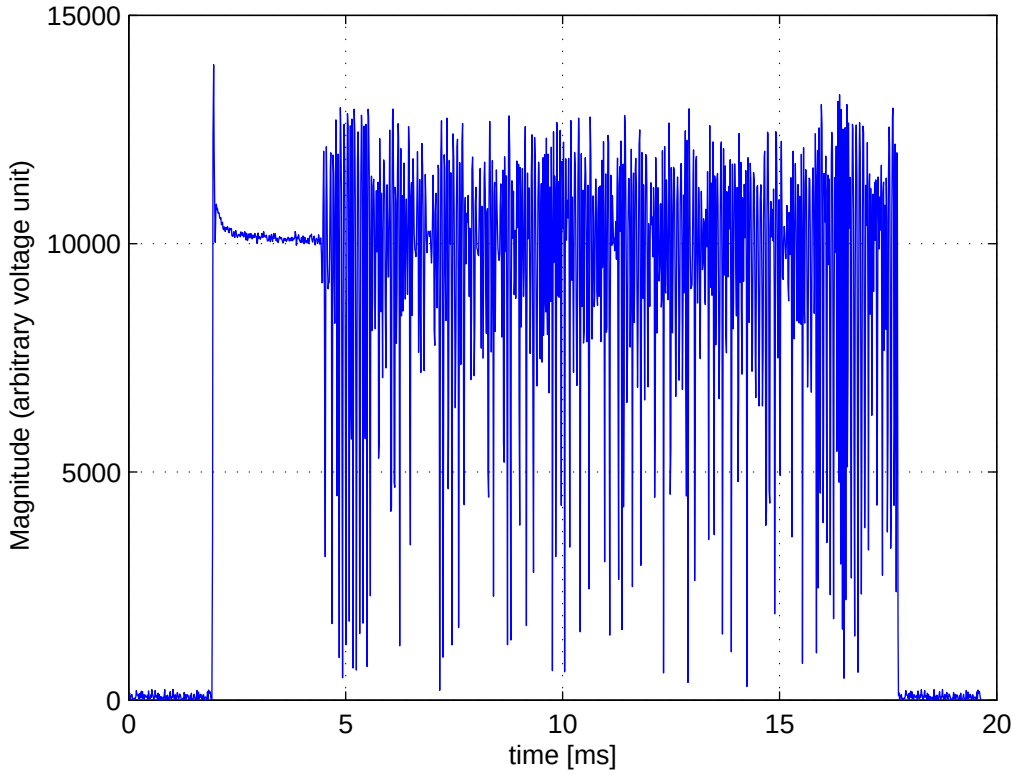

Figure 3.7: Observed Iridium downlink burst waveform (magnitude)

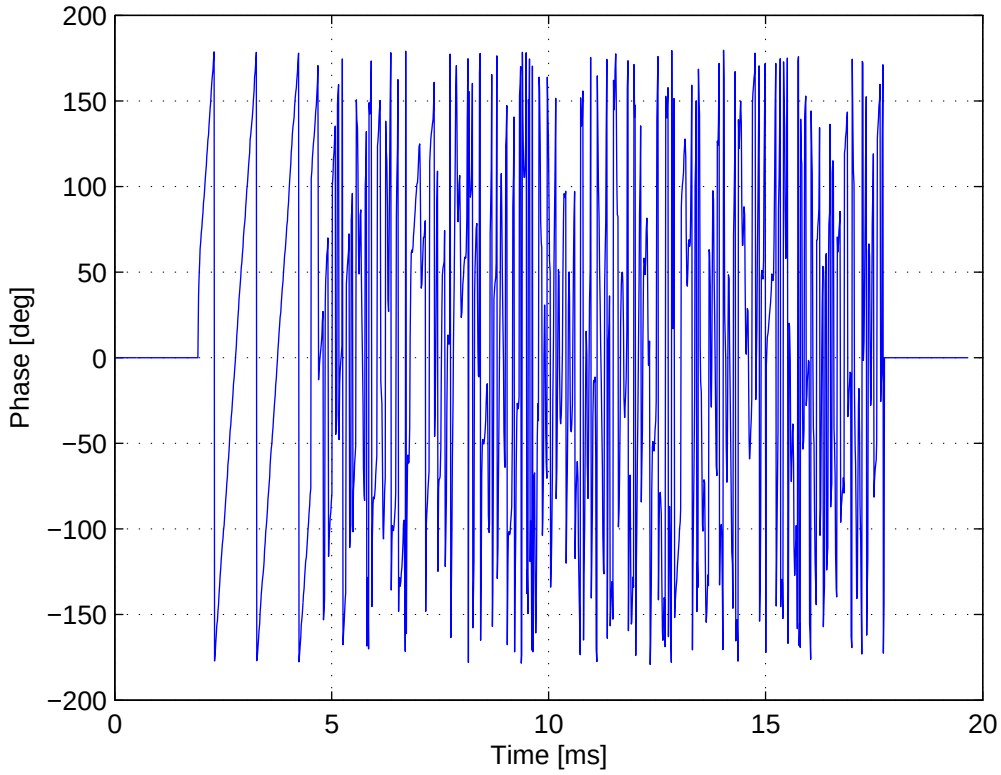

Figure 3.8: Observed Iridium downlink burst waveform (phase)

Chapter 4

Algorithm

In this chapter, a data model for Iridium downlink signal as well as a technique to mitigate the interference caused by this signal to radio astronomy are presented. In Section 4.1, the data model for the downlink signal is presented. Section 4.2 contains the proposed algorithm and a high level block diagram of the proposed algorithm. In Section 4.3, details of each block is described. In Section 4.4, a detailed description of how the algorithm was implemented is presented.

4.1 Data Model

The Iridium downlink signal appears burst by burst and the typical size of a burst is 10's of milliseconds. Iridium downlink signals have a bandwidth of 41.67 kHz per channel. Iridium signals can be considered as narrowband signals as the signal bandwidth is small compared to the frequency scale of channel variations. A mathematical model for the signal transmitted from an Iridium satellite is:

$$s_t(t, \omega_c) = b(t - \eta)e^{j(\omega_c t + \theta)} \tag{4.1}$$

where $b(t)$ represents transmitted data symbols, ω_c is the center frequency upon transmit, and θ represents an arbitrary phase introduced during modulation. The true radio frequency (RF) signal is the real part of the signal represented in the Equation (4.1). Since the timing of symbol transitions is not known *a priori*, an unknown time offset η is introduced. The signal received by the radio telescope can be written as

$$s_r(t) = G(t)P(t)s_t(t - \eta - \tau_{pt}, \omega_c + \omega_d) \tag{4.2}$$

where ω_d represents the frequency shift due to Doppler effect, τ_{pt} represents propagation time, $G(t)$ is the radio telescope response, and $P(t)$ is the response of the propagation channel which includes path loss. $G(t)$ includes the antenna response, the feed response, and the receiver response.

Narrowband signals received from satellites typically exhibit negligible (or resolvable) multipath effect, thus $P(t)$ can be modeled as a single time-varying complex coefficient. $G(t)$ can also be modeled as single time-varying complex coefficient as Iridium signal has narrowband characteristics. Thus $P(t)G(t) = \alpha$

From Equation (4.1) and (4.2), this signal can be written as

$$s_r(t) = \alpha b(t - \eta - \tau_{pt}) e^{j[(\omega_c + \omega_d)(t - \tau_{pt}) + \theta]} \tag{4.3}$$

We now define two new variables: $\tau = \eta + \tau_{pt}$ as well as $\omega = \omega_c + \omega_d$, and rearrange Equation (4.3), then we get

$$s_r(t) = \alpha e^{-j\omega\tau_{pt}} e^{j\theta} b(t-\tau) e^{j\omega t} \tag{4.4}$$

Now, the received signal can be described in terms of three unknown parameters: ω, τ, and a single slowly varying complex constant $A = \alpha e^{j(-\omega_c \tau_{tp} + \theta)} e^{-j\omega_d \tau_{tp}}$. The expression for the received signal can thus be written as

$$s_r(t) = Ab(t-\tau) e^{j\omega t} \tag{4.5}$$

The channel on receiver is assumed to corrupt the signal by the addition of noise. The noise introduced is modeled as additive white Gaussian noise (AWGN) with zero mean. The model of noisy version of the received signal is written as

$$s(t) = Ab(t-\tau) e^{j\omega t} + n(t) = s_r(t) + n(t) \tag{4.6}$$

where $n(t)$ denotes additive white Gaussian noise(AWGN) [17].

4.2 Proposed Algorithm

A technique is presented here to mitigate the interference caused by the downlink signal of the Iridium to L-band radio astronomy. The strategy of proposed algorithm is to detect the interfering signal, create a replica of it and then subtract it from the signal received by radio telescope. Figure 4.1 shows a high level block diagram of the proposed algorithm.

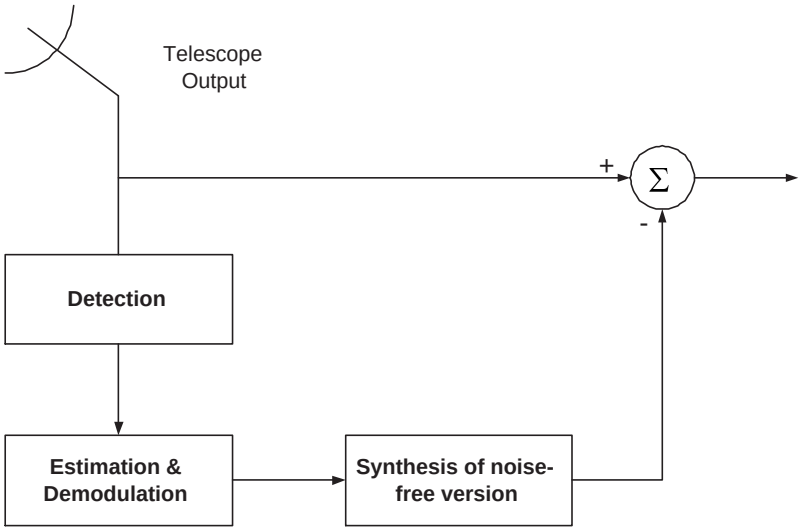

Figure 4.1: High level block diagram of the proposed algorithm

The proposed algorithm contains three phases: (1) detection, (2) estimation and demodulation, and (3) synthesis of a noise-free version. The first phase of the proposed algorithm is detection of a signal burst. The second phase is to estimate the unknown parameters of the signal burst and demodulate it. The third phase is to remodulate and reconstruct the Iridium signal burst using only the estimated parameters. Finally, the reconstructed signal is subtracted from the telescope output, thereby canceling the original burst. This process is repeated for each burst detected.

4.3 Details of The Algorithm

In the previous section, a high level diagram of the algorithm was presented. The intent of this section is to provide the details of each block of the diagram.

4.3.1 Burst Detection

With respect to the signal model of Equation (4.6), the optimum detector of the tone burst is a filter matched to the transmitted tone burst, followed by a threshold test [18]. The value of the threshold determines the false-alarm rate (FAR). The value of the threshold is user-selectable and it is set to the smallest value that yields an acceptable false-alarm rate (FAR). The procedure to detect signal is as follows:

1. The output of the matched filter is computed as:

$$y(t) = h(t) * x(t) \tag{4.7}$$

where $y(t)$ is the output of matched filter, $h(t)$ is the impulse response of the filter, $x(t)$ is the matched filter input $= |s(t)|$. As usual "$*$" denotes as convolution. The implementation procedure of Equation (4.7) and determining matched filter coefficients is presented in Section 4.4.1.

2. The "local" mean m and standard deviation σ of $y(t)$ is then computed. The samples used to compute the mean and standard deviation should not contain any burst. As we know the start of the burst and the time separation between bursts (90 ms), we can calculate noise by taking data in between burst and then we can calculate m and σ.

3. A detection is declared when $y(t) - m >= \beta\sigma$, where β is the user-selected threshold that sets the FAR.

It is known that this detector yields optimal solution in absence of multipath and in presence of AWGN. The threshold of the detector is user-selectable and it is set to the smallest value that yields desirable false-alarm rate (FAR). However, there is a trade-off between the value of β and the detection sensitivity. By increasing β sufficiently high, one can ensure that the maximum acceptable FAR is never exceeded; but this process will degrade the detection sensitivity [11].

4.3.2 Signal Estimation and Demodulation

Once a burst is detected, estimation or acquisition of unknown parameters have to be conducted before demodulating the signal. Figure 4.2 shows a block diagram of this process.

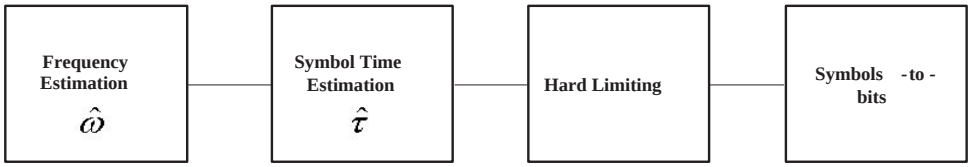

Figure 4.2: Block Diagram of Estimation and Demodulation

Several different signal processing methods exists to determine the center frequency ω_c. The Iridium downlink signal is a modulated complex exponential; an optimum estimator for estimating center frequency is a maximum likelihood estimator (MLE) of the frequency [19]. It is known that the optimal estimate $\hat{\omega}$, the frequency of a complex exponential function, is:

$$\hat{\omega} = \arg\max_{\omega} \frac{1}{N}\left|\sum_{n=0}^{N-1} x[nT_s]e^{-j2\hat{\omega}nT_s}\right|^2 \tag{4.8}$$

where $x[nT_s]$ is the received signal, $\hat{\omega}$ is the frequency estimate. This is the optimal estimator and hence no other algorithm is needed to estimate frequency.

A simple suboptimal method to estimate the center frequency is to identify the peak of the FFT of the signal. The exact center frequency can not be found in this method due to the limited resolution of the FFT. However, it can be said that the center frequency lies within one bin width of the bin that has the peak of the FFT [20]. This knowledge can be used to narrow the range of the brute force search in Equation (4.8).

The frequency factor can be removed by multiplying S_r by $e^{-j\hat{\omega}t}$. This will yield the following lowpass baseband signal

$$S_{rb} = Ab(t - \tau) \tag{4.9}$$

The process of estimating the unknown value τ is called symbol timing recovery. Symbol timing recovery the can be achieved in several ways. A simple but effective method is presented in Section 4.4.3.

Once the symbol timing is recovered, the existing data samples have to be re-sampled with the estimated symbol timing. This conversion of sample rate can be done simply by exploiting Nyquist's Sampling Theorem [21]. The sampling theorem

says that samples of a signal with a desired sampling period P can be reconstructed from another signal sampled at period T as follows

$$x(mP) = \sum_{n=-\infty}^{n=\infty} x[nT] \frac{sin[\frac{\pi}{T}(mP - nT)]}{\frac{\pi}{T}(mP - nT)} \tag{4.10}$$

Thus

$$x(mP + \tau) = \sum_{n=-\infty}^{n=\infty} x[nT + \tau] \frac{sin[\frac{\pi}{T}(mP - nT)]}{\frac{\pi}{T}(mP - nT)} \tag{4.11}$$

where m is the sample index of new signal, and n is the sample index of old signal. A simple filter can constructed to perform this operation. With this symbol timing adjustment, Equation (4.9) will become

$$S_{rb} = Ab(t) \tag{4.12}$$

where the signal is resampled with period P.

A broad class of signals has a property known as constant modulus, which means that all their information is conveyed using phase variations, and their magnitude is normally constant. Signals falling into this category include analog FM and digital signals using phase-shift keying such as the Iridium signal. In this type of signal, hard

limiting can be performed before demodulation. Hard limiting improves the performance of demodulation as it has the effect of suppressing the magnitude component of the noise [22]. After hard limiting, the symbols of the received signal lie on the unit circle and are only phase-shifted versions of transmitted symbols, which can then be easily demodulated using traditional demodulation techniques.

4.3.3 Signal Remodulation and Reconstruction

Once the estimation of all the essential unknown parameters and demodulation of the symbols are completed, remodulation and synthesis phase can be implemented. Figure 4.3 shows a block diagram of this process. Only the key stages are presented here. Details of the process is presented in Section 4.4.

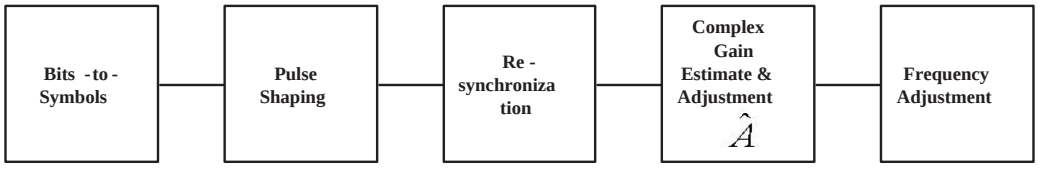

Figure 4.3: Block Diagram of Remodulation and Synthesis

In this phase, demodulated symbols are remodulated at first. Remodulated signals are then pulsed shaped. The next phase is resynchronization phase. The objective of resynchronization phase is to synchronize the recreated signal with the received signal. Three degrees of synchronization is needed - matching the sample frequency of synthesized signal with received signal using Nyquist's filter described in Section 4.3.2, reintroduce symbol time delay τ to match with symbol time delay of the received signal, and compensate the delay of synthesized signal which was introduced during

filtering process. The frequency factor can be introduced simply multiplying the synthesized signal by $e^{j\hat{\omega}t}$. This will yield a bandpass signal

$$\hat{s}(t) = b(t - \hat{\tau})e^{j\hat{\omega}t} \tag{4.13}$$

One important unknown parameter not estimated during the "estimation and demodulation" phase is complex magnitude. In order to do so, let us look at the received signal which can be written as

$$x(t) = As(t) + n(t) \tag{4.14}$$

where $s(t)$ is the symbol and A represents a combined complex gain which takes account of all the effects.

Let us assume the synthesized noise-free signal is $\hat{x}(t)$. Cross correlation with the received signal $x(t)$ gives:

$$r_x = \int x(t)\hat{x}^*(t)dt \tag{4.15}$$

$$r_x = \int [As(t) + n(t)]\hat{s}^*(t)dt \tag{4.16}$$

$$r_x = A\int s(t)\hat{s}^*dt + \int n(t)\hat{s}^*(t)dt \tag{4.17}$$

Let us assume $r_s = \int s(t)\hat{s}^*(t)dt$ and $n_s = \int n(t)\hat{s}^*(t)dt$. The value of n_s is ideally zero. Hence, the complex gain A is

$$\hat{A} = \frac{r_x}{r_s} \tag{4.18}$$

The unknown parameter A can be easily calculated from Equation (4.18). So the final version of the noise-free signal is

$$\hat{s}(t) = \hat{A}b(t - \hat{\tau})e^{j\hat{\omega}t} \tag{4.19}$$

4.3.4 Cancelation

The remodulated and reconstructed signal then can be subtracted from the original signal to achieve proposed cancelation.

4.4 Algorithm Implementation

In last couple of sections, the algorithm to mitigate interference is proposed and the rationale is explained. The intent of this section is to present a more detailed description of the implementation of the proposed algorithm. Figure 4.4 shows exact steps used during the implementation of estimation and demodulation phase. Figure 4.5 shows exact steps used during the implementation of the remodulation and synthesis phases.

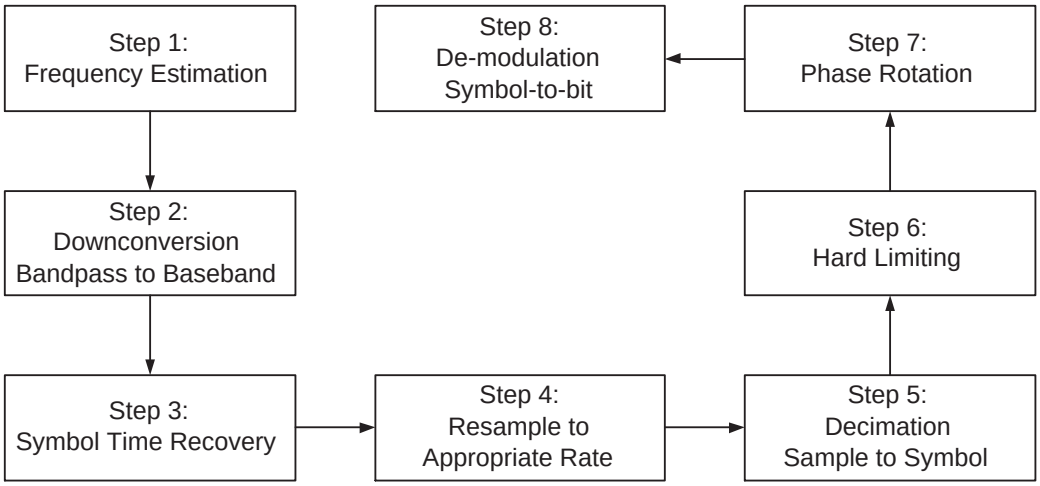

Figure 4.4: Implementation of signal estimation and demodulation

4.4.1 Detection

A matched filter based detector followed by a threshold test is implemented here based on the algorithm presented in Section 4.3.1. As the shortest Iridium tone burst observed is about 8 ms, the length of the matched filter is set to 8 ms. Filter coefficients determining procedure is shown below with an example.

Example

Let the sample rate $F_s = 1000$ SPS and length of the filter $L = 8$ ms $= 0.008$ and coefficients of the filter are a and b. The coefficients is calculated as:

$$M = F_s \times L = 1000 \times 0.008 = 8, So \tag{4.20}$$

$$h\left(\frac{k}{F_s}\right) = \frac{1}{M}[1\ 1\ 1\ 1\ 1\ 1\ 1\ 1] \tag{4.21}$$

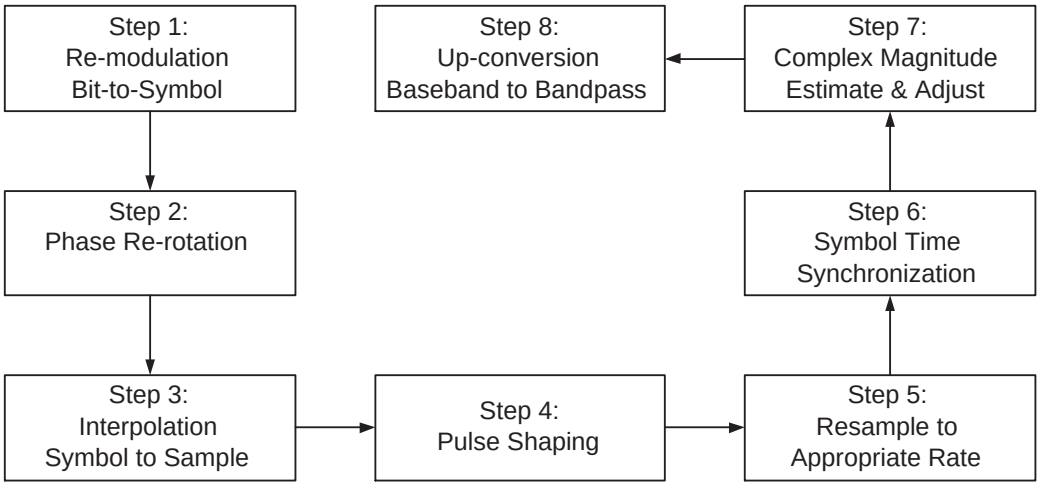

Figure 4.5: Implementation of remodulation and synthesis of noise-free signal

4.4.2 Frequency Estimation

A Maximum likelihood estimator (MLE) is implemented here to estimate the frequency. The estimator is given in Equation (4.8).

4.4.3 Symbol Time Estimation

A differential detection of symbol timing is implemented here. Differential detection of symbol timing is advantageous in communications systems where fast synchronization is required. Differential detection does not require carrier recovery. The theory of symbol timing presented here is based on simple squaring/energy comparison technique [23]. The energy of a sample is calculated simply by

$$e = x_k^2 + y_k^2 \tag{4.22}$$

where x_k and y_k represents respectively the real and imaginary part of the kth sample.

For example, let us assume four samples per symbol. In order to implement this method for four samples per symbol, four shift registers is needed. Each shift register holds one of every four samples that represent a symbol. For example, if the shift registers are 4 samples long, then first shift register will hold first, fifth, ninth and thirteenth samples of the data stream. At each clock cycle, the total energy of the samples stored is calculated and compared to the other registers. This process continues for the entire data stream. Figure 4.6 shows a block diagram of symbol time recovery algorithm. Figure 4.7 shows the total energy stored in each shift register at a time for entire sweep.

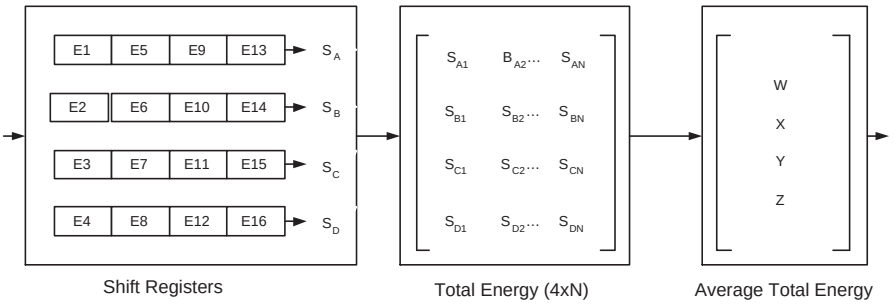

Figure 4.6: Block diagram of symbol time recovery process

The symbol timing τ then can be calculated from the lag spectrum of sample (offset) times by assuming lag spectrum of sample (offset) times as a triangle function. For example, let W, X, Y, and Z respectively stand for highest, second highest, third highest, and lowest total average energy. A close look reveals that the sample (offset) times can be modeled as a triangle function. Now if we look at sample (offset) times, we can get optimum $\hat{\tau}$, which is the peak of the triangular lag spectrum. But here in this thesis, the highest total average energy W is taken as $\hat{\tau}$. This is suboptimal and

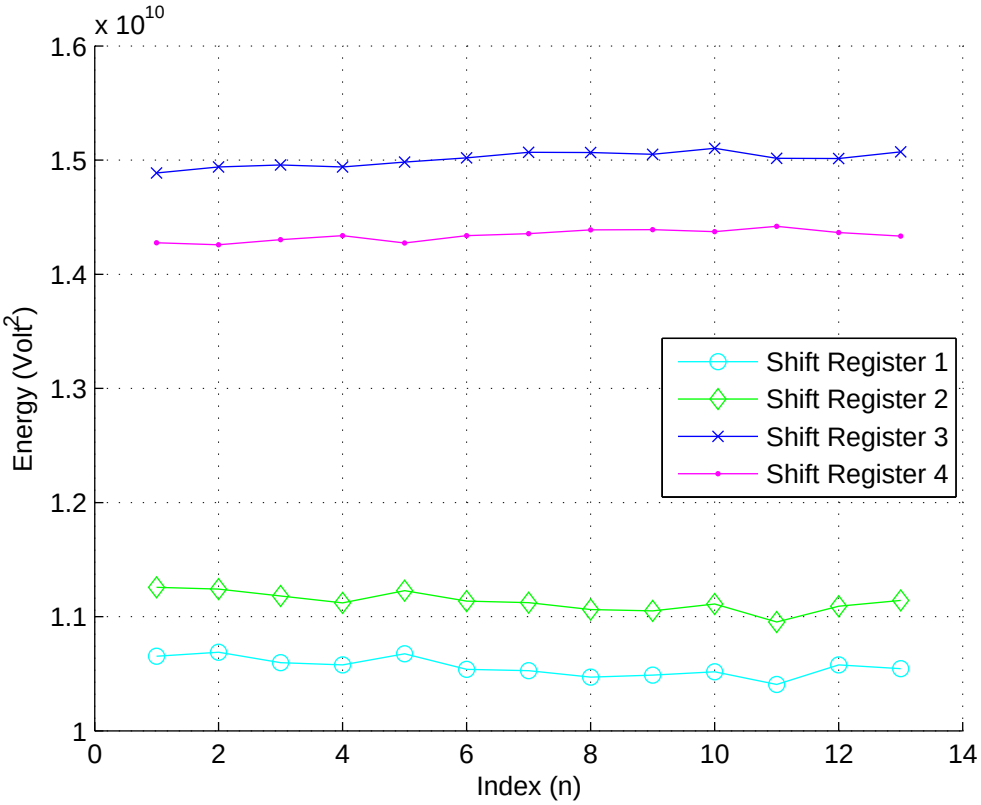

Figure 4.7: Total energy stored in shift registers during symbol time recovery process. In this case $\hat{\tau}$ lies between the delays associated with registers 3 and 4.

certain to degrade the performance. Figure 4.8 shows an example of lag spectrum where the peak value is optimum $\hat{\tau}$ and $\hat{\tau}$ for W is the highest among all four values, which is taken as symbol time delay.

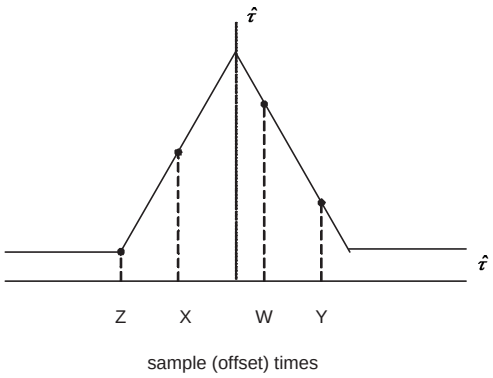

Figure 4.8: Symbol time recovery process: lag spectrum

4.4.4 Resampling

Once the symbol time τ is recovered, the data samples have to be adjusted for this symbol timing. Also note that the algorithm will be implemented here to recover the symbol timing requires an integer number of samples per symbol (in our case four samples per symbol). If the data used here is not an integer multiple of the symbol, then this algorithm will not work. In that case, we need to convert the data sample rate to desired four samples per symbol. Both of these goals can be achieved by implementing a simple resampling filter. The filter can be constructed using Nyquist's Sampling Theorem as shown in Equation (4.10).

4.4.5 Decimation

After symbol time recovery and resampling, it is assumed that the signal has four samples per symbol. Three out of every four samples can be discarded and still we will be able to demodulate. This process is known as decimation [24]. The sample that has highest energy is selected. For example, in Figure 4.7, shift register 3 has higher value than any other shift register. Shift register 3 contains third, seventh, and so on. So taking the sequence of third, seventh sample will yield symbols with highest energy thus enable us to demodulate all the symbols with less bit error.

4.4.6 Hard Limiting

Hard limiting has to be performed before demodulation which means to force each sample of data stream onto the unit circle. This removes any amplitude variation. Hard limiting can be achieved simply by dividing each sample by its magnitude.

4.4.7 Phase Rotation and Rerotation

The propagation channel introduces arbitrary phase shift in the signal. Phase rotation must be performed before demodulation to rectify this phase shift so that symbols remain in the appropriate quadrant in signal space. Phase rotation can be implemented simply multiplying the signal by $e^{j\theta}$, where θ is the arbitrary phase introduced during propagation. A correlation between known unique word and received signal yields this phase angle, θ. Same amount of the phase rotation needs to be introduced during remodulation phase.

4.4.8 Demodulation and Remodulation

Utilizing this prior knowledge about the modulation scheme used, simple hard decision decoding is implemented here. Extracted bits were then remodulated. Unique word bits are modulated using BPSK modulation scheme and information bits are modulated using QPSK modulation scheme. Note that Unique Words are used for channel and timing estimation, and can, in some burst profiles. Key characteristics of a Unique Word are that it has good periodic correlation properties, and thatits symbols have a constant amplitude. The BPSK unique word is shown below

$$0\ 0\ 0\ 0\ 1\ 1\ 1\ 0\ 1\ 1\ 0\ 0\ 1\ 1\ 0\ 1\ 0\ 0\ 1\ 1\ 0\ 0\ 1\ 0\ 1\ 1\ 0 \tag{4.23}$$

4.4.9 Interpolation and Pulse Shaping

Next stage is to upsample the synthesized symbols to multiple of symbol frequency and then pulse shape the synthesized signal.

Interpolation

Interpolation is a process where the sample rate is increased. There are several methods of up-sampling: zero-insertion, zero-order-hold (ZOH), zero-insertion and raised-cosine filtering, and fast Fourier transform (FFT) expansion [22]. Zero-insertion is probably the most streightforward method for interpolation. Figure 4.9 shows direct implementation of a zero-insertion interpolator in time domain.

In this method, zeros are inserted between samples of the original signal. This yields a new signal which is then passed through a low-pass filter. This process creates

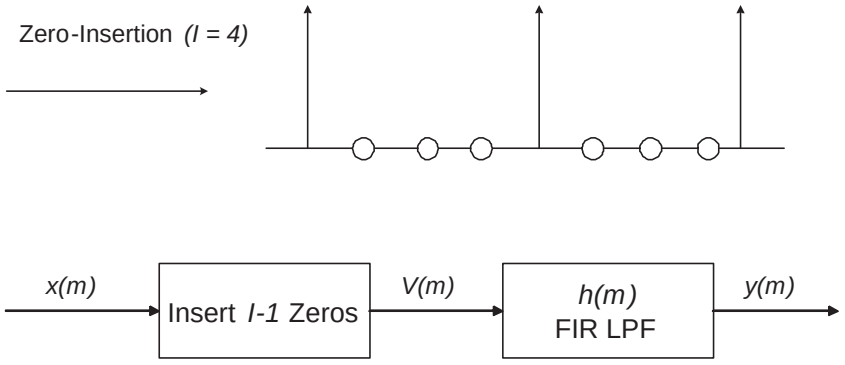

Figure 4.9: Zero-insertion interpolator in time domain

a signal which is just an upsampled version of the original signal. In Figure 4.9, the up-sampling factor I is 4 and $I-1$ zeros are inserted between each pair of consecutive samples of the original signal.

Pulse Shaping

When the pulse for each symbol passed through a band-limited channel, it smears into the time interval of the succeeding signal. This phenomenon is commonly known as intersymbol interference (ISI), which eventually leads to an increased probability of error in detecting a symbol. Improvement is possible by shaping the symbol pulse in such a way that at every sampling instance at the receiver, the response due to all symbols except the current symbol is equal to zero [25].

Several different pulse shaping filters is known which serves the purpose such as raised cosine, root raised cosine, Gaussian pulse shaping filter. One of the most popular pulse shaping filter used in wireless communication systems is the root raised cosine filter. This filter is also used in Iridium signals. Figure 4.10 shows the impulse response of a typical root raised cosine filter.

The impulse response of the root raised cosine filter is given as:

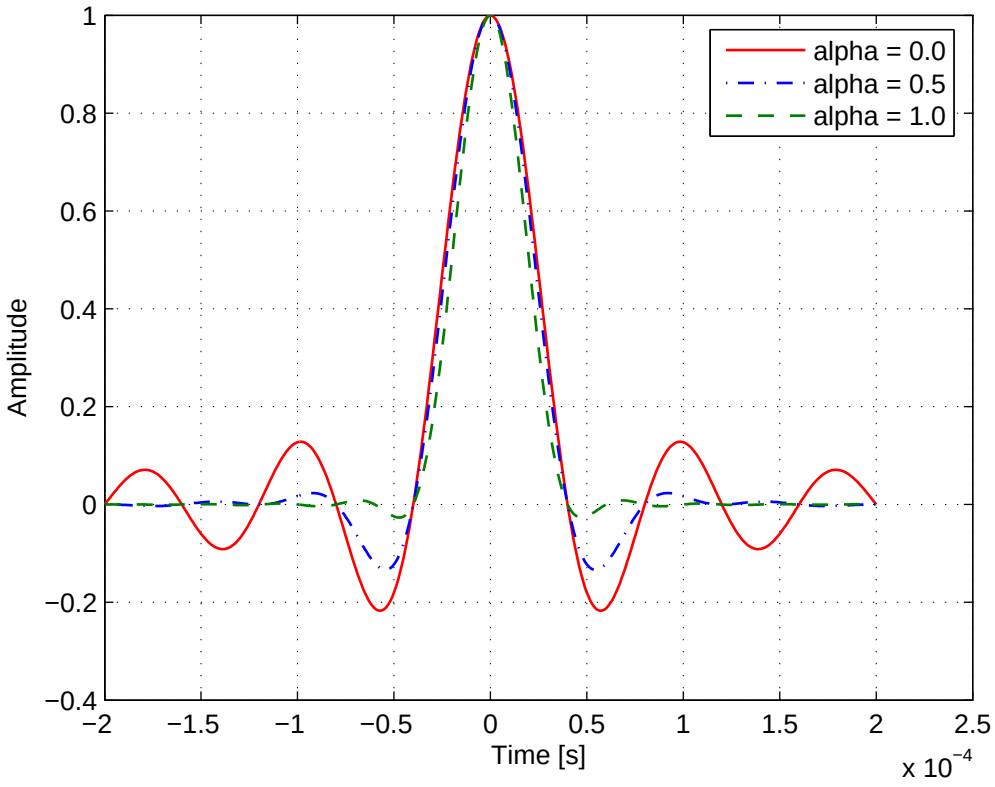

Figure 4.10: Impulse response of a typical root raised cosine (RRC) filter

$$h(t) = \frac{4\alpha}{\pi\sqrt{(T)}} * \frac{cos(\frac{(1+\alpha)\pi t}{T}) + \frac{T}{4\alpha t} * sin(\frac{(1-\alpha)\pi t}{T})}{1 - (4\alpha\frac{t}{T})^2} \tag{4.24}$$

where T is the symbol interval, α is a rolloff factor (excess bandwidth)[22]. A discrete time pulse-shaping filter, i.e. FIR filter, is obtained from $h(t)$ by taking samples at regular time intervals $\frac{1}{Fs}$. The sampling frequency Fs depends on, e.g., a system bandwidth and symbol rate $\frac{1}{T}$.

Zero-insertion and Pulse Shaping

The "Zero-insertion" technique is adopted here for interpolation and "root raised cosine filtering" technique is adopted here for shaping the pulse. Combining two simplifies the overall design. Figure 4.11 shows an example of this application.

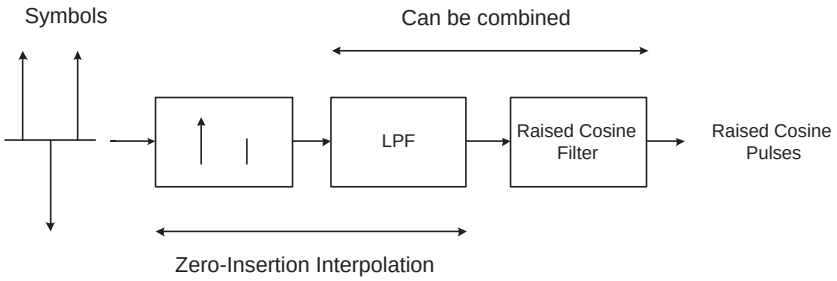

Figure 4.11: A combined method of interpolation and pulse shaping

This combination is performed by using the zero-insertion interpolation technique mentioned earlier. One notable difference is the lowpass filter can be replaced by a raises-cosine filter. As raised-cosine filter has smaller bandwidth than interpolating LPF, the low-pass filter can be ignored. As a whole the process can considered as a single filter that does both pulse shaping and interpolation [22].

4.4.10 Symbol Time Synchronization and Resampling

The interpolated and pulse-shaped synthesized signal is then synchronized in time and resampled at appropriate rate. Both symbol time synchronization as well as resampling can be implemented at the same time using a simple FIR filter based on Nyquist's Sampling Theorem. The same filter was developed and used during demodulation phase.

4.4.11 Complex Magnitude Estimation and Adjustment

The unknown complex magnitude A can be calculated easily. The outcome of cross-correlation between received signal and estimated signal will yield the desired A.

4.4.12 Frequency Adjustment

Up to now, the synthesized signal is baseband. It needs to be up-converted to a bandpass signal. The frequency factor can be introduced simply multiplying this estimated signal by $e^{j\omega t}$.

4.4.13 Cancelation

At this stage, reconstructed signal is an estimated replica of the original signal. This reconstructed signal can be subtracted from the telescope output to achieve proposed cancelation. The performance of the proposed algorithm is presented in Chapter 5 and Chapter 6.

Chapter 5

Algorithm Validation by Simulation

In this chapter, the rationale of using simulation to validate the proposed algorithm as well as the results obtained from the simulation is presented. In Section 5.1, the desirability of using simulation to validate proposed algorithm is presented. In Section 5.2, the simulation methodology is presented. In Section 5.3, the performance of detector is presented. In Section 5.4, different aspects of canceling performance is presented assuming perfect detection. In Section 5.5, performance of the complete proposed algorithm is presented. In Section 5.6, a comparison is presented of performance using two methods: (1) Detect/Blank, and (2) Detect/Cancel.

5.1 Desirability of Modeling Using Simulation

In this chapter, we will create a simulated Iridium data, then pass it through AWGN channel, and finally use these artificial data to validate the proposed algorithm.

5.2 Simulation Procedure

In this section, a detailed description of simulation procedures and parameters are presented. At the beginning of the simulation, a simulated Iridium dataset is generated. Like real Iridium signals, simulated signal has three segments: (1) CW preamble (tone burst), (2) BPSK-modulated unique word, and (3) QPSK-modulated data. The symbol rate of the data used in simulation is 25 kSy/s. The burst is pulse shaped by a root-raised cosine (RRC) filter with rolloff factor of 0.4 and upsampled to 100 kSPS. In order to simulate the data analyzed in Chapter 6, the upsampled data is then converted to a 78.125 kSPS dataset.

It is assumed that the simulated burst contains no multipath effect as well as no other real life channel effect. In order to simulate different scenario with variable signal to noise power ratio (SNR), AWGN with different power were introduced while keeping signal level fixed. The range of SNR of simulated data considered here are from -10 dB to $+20$ dB.

5.3 Detection Performance

In this section, the performance of the detector is presented. Figure 5.1 shows the detection sensitivity for $\beta = 5$ and $\beta = 10$. Note that β is user-selectable threshold that sets the FAR. In this simulation, the results are generated with $m(t)$ and $\sigma(t)$ held fixed at their nominal 'noise only' values. The sensitivity of the detector depends on the value of β. Sensitivity of the detector increases with the decrease of β. In Figure 5.1 , it can be seen that the detector can detect burst with lower SNR at $\beta = 5$ than at $\beta = 10$, which means the detector is more sensitive to the burst at $\beta = 5$

than at $\beta = 10$.

However, as the detector becomes more sensitive to burst, the FAR grows higher. Higher β is desired to keep the FAR low. So, there is trade-off between detection sensitivity and FAR. Also note that due to the 'processing gain' associated with the matched filter, the detector is able to detect the burst that are much weaker than the noise.

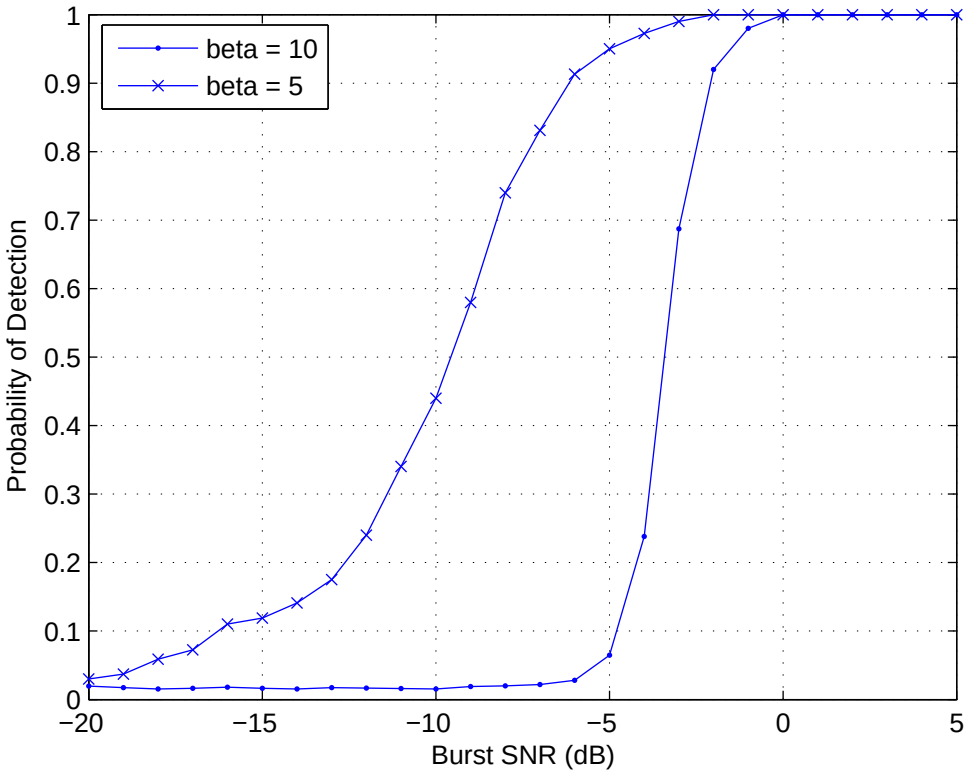

Figure 5.1: Burst detection performance with varying β

5.4 Canceling Performance

In this section, the canceling performance of the proposed algorithm is observed and analyzed. Performance for a high and an intermediate signal to noise ratio is presented here. A signal that has 20 dB SNR is considered here as high SNR signal; and for intermediate SNR case, a signal with 10 dB SNR is used. Time domain and frequency domain results are presented here for both cases. Suppression vs. SNR performance is also presented here which shows the variation of cancelation performance with SNR.

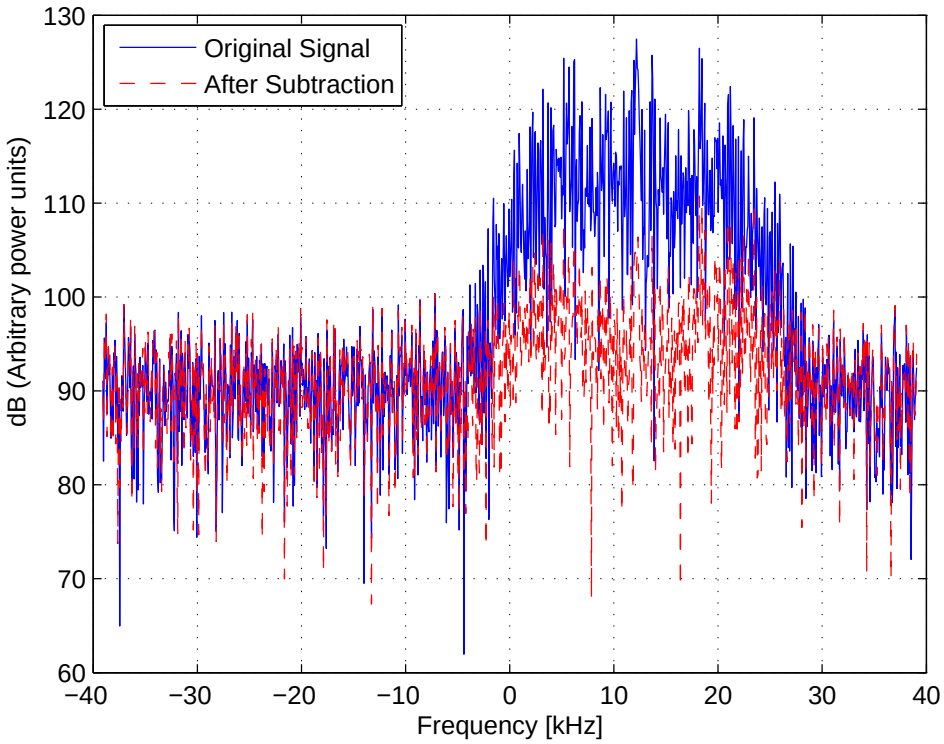

Figure 5.2: Single burst with 20 dB SNR (in frequency domain)

Figure 5.2 and 5.3 respectively shows frequency domain and time domain representation of signal with 20 dB SNR. Note that the signal has complex value and thus

it is asymmetric is frequency domain. It can be observed that the proposed interference mitigation scheme achieves 14 dB of suppression for 20 dB SNR, assuming perfect detection. Figure 5.4 and 5.5 shows respectively frequency domain and time domain representation of signal for 10 dB SNR. It can be observed that the proposed interference mitigation scheme achieves 8 dB of suppression for 10 dB SNR, assuming perfect detection. Notice that the canceling performance increases with the increase of SNR as with increase of SNR, since it is possible to estimate the parameters and demodulate the symbols more accurately.

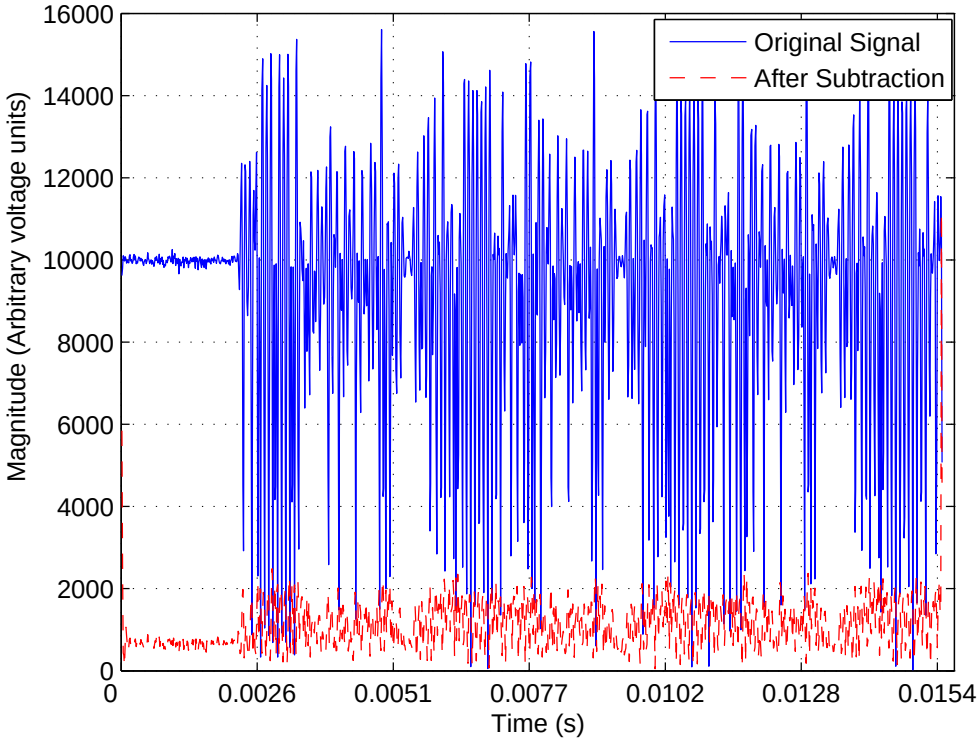

Figure 5.3: Single burst with 20 dB SNR (in time domain)

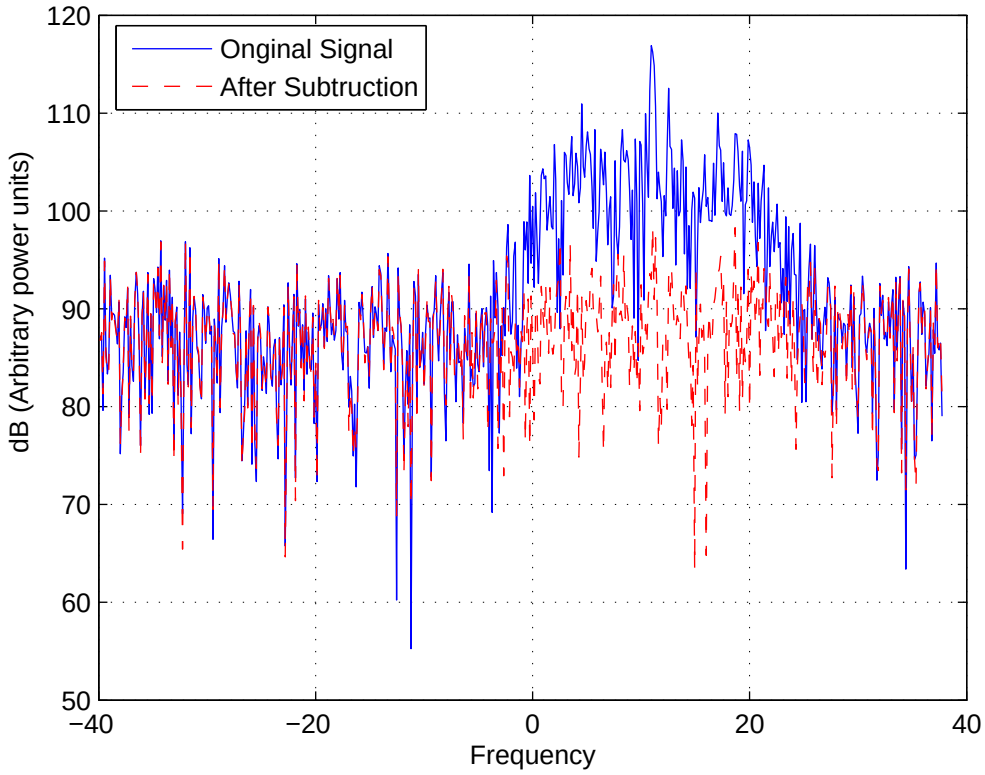

Figure 5.4: Single burst with 10 dB SNR (in frequency domain)

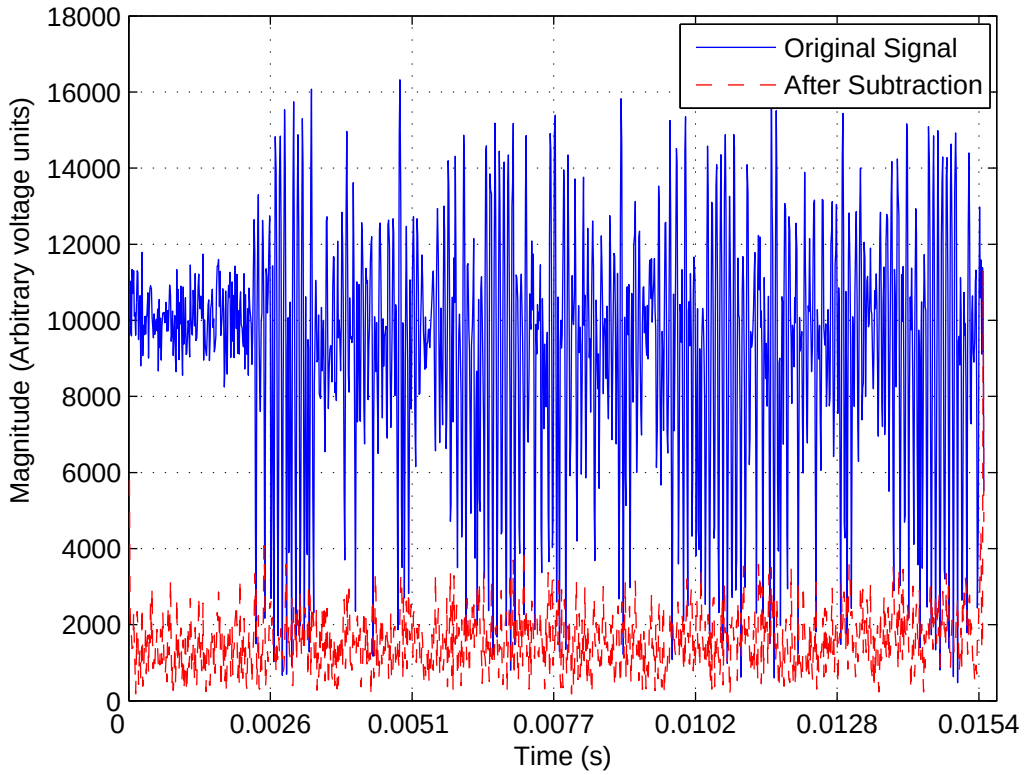

Figure 5.5: Single burst with 10 dB SNR (in time domain)

Figure 5.6 shows the canceling performance with varying SNR. The range of SNR used here varies from 0 dB to 30 dB. Figure 5.6 shows that the proposed algorithm achieves about 1.4 dB suppression for SNR equal to 0 dB, 8 dB suppression for SNR equal to 10 dB, and 14 dB suppression for SNR equal to 20 dB. It can be observed that the suppression rate grows faster at low SNR and the rate of change reduces at relatively high SNR. For example, suppression changing rate is faster at SNR from 0 dB to 10 dB; in between SNR 15.0 dB to 20 dB, it appear to converge at about 18.0 dB suppression. The key reason for performance convergence is the error in symbol timing. The method implemented here is suboptimum which leads to a erroneous

estimation of symbol time. This eventually degrades the performance regardless of signal strength. At high SNRs (for example, at 15 to 20 dB), the signal strength is already sufficient enough to estimate the parameters and demodulate the symbols accurately, but the suboptimal symbol time estimation is always there. Therefore, at high SNR cases, the level of accuracy of estimation and symbol demodulation correctly does not change much with increase of SNR. So the canceling performance doesn't change either.

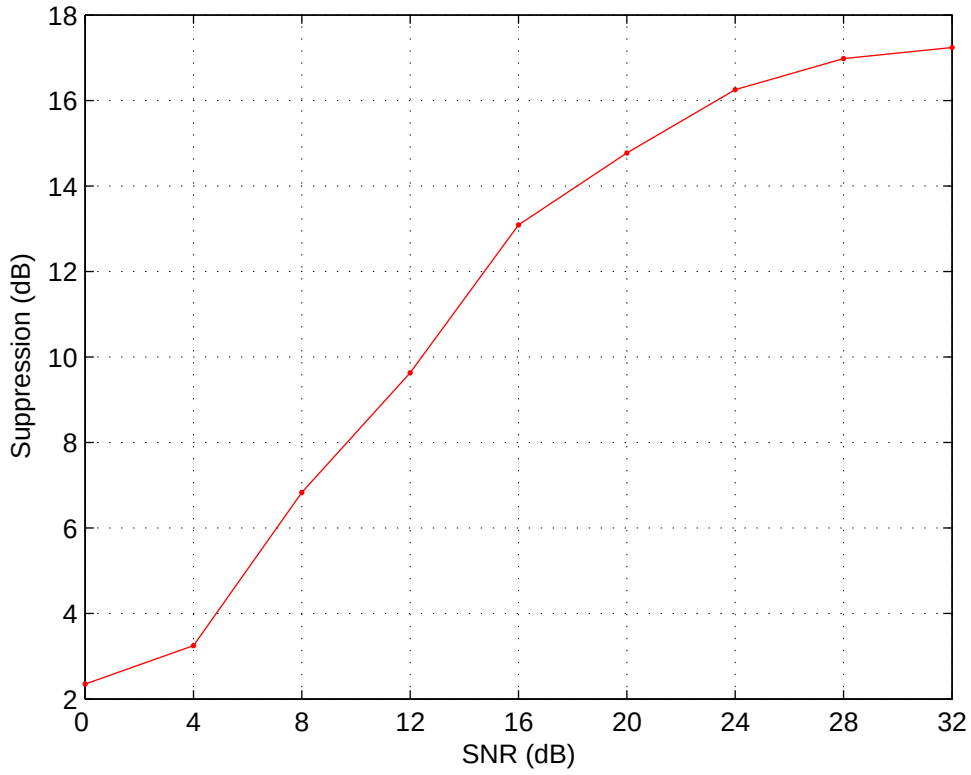

Figure 5.6: Suppression (dB) vs. SNR Performance

5.5 Complete System Performance

This section includes complete system performance of the proposed algorithm - from detection to cancelation.

5.5.1 Detection

In this section, the performance of the detector is presented using a dataset that contains a single burst and Figure 5.7 and Figure 5.8 respectively shows that received signal and the magnitude of the detector output. Figure 5.9 shows a single simulated data file and the detector. The start and the end of burst can be found from the threshold, β. Figure 5.10 shows the detected burst of a Iridium satellite signal. Time domain representing of the burst vs. sample index is presented here.

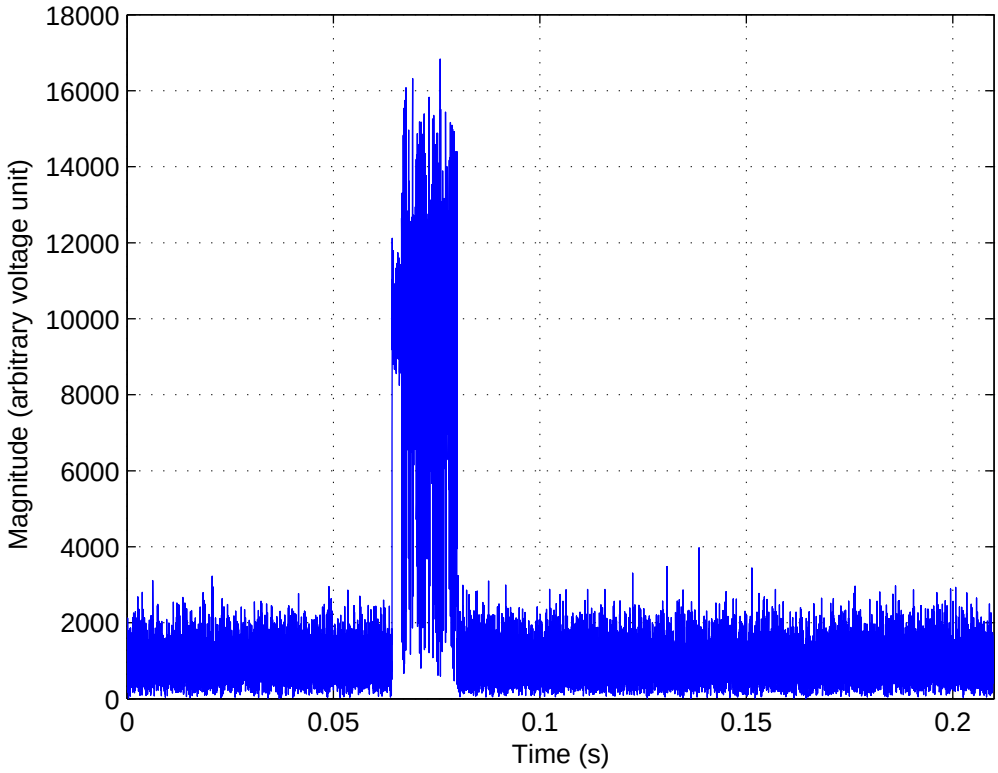

Figure 5.7: Magnitude of the received data

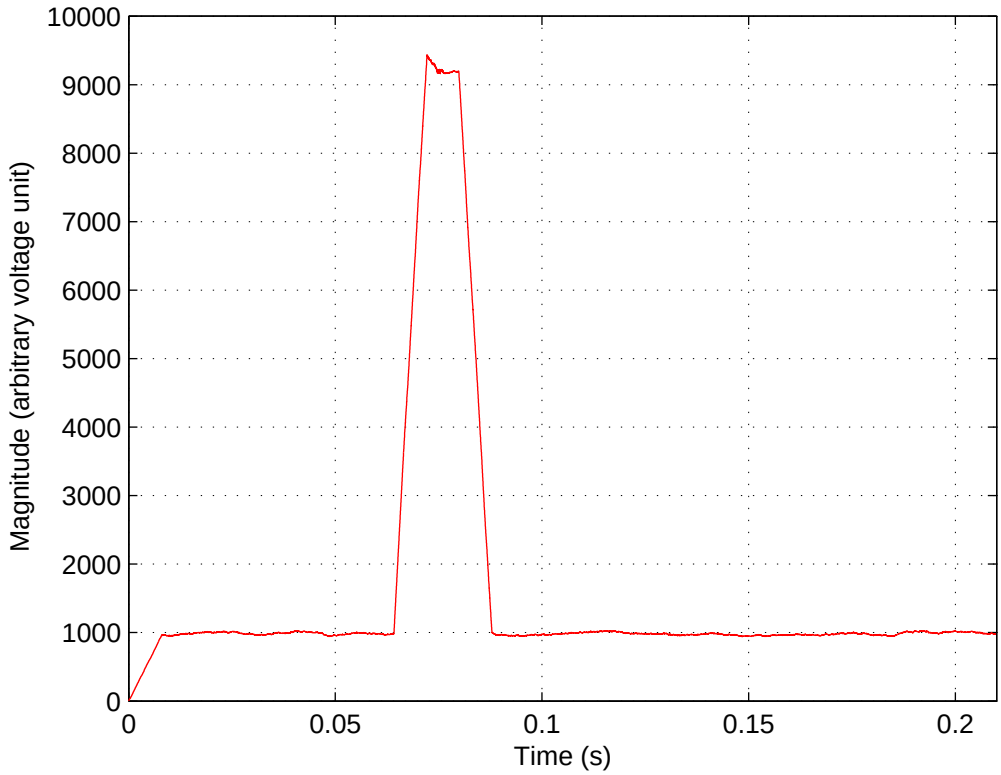

Figure 5.8: Magnitude of the detector output

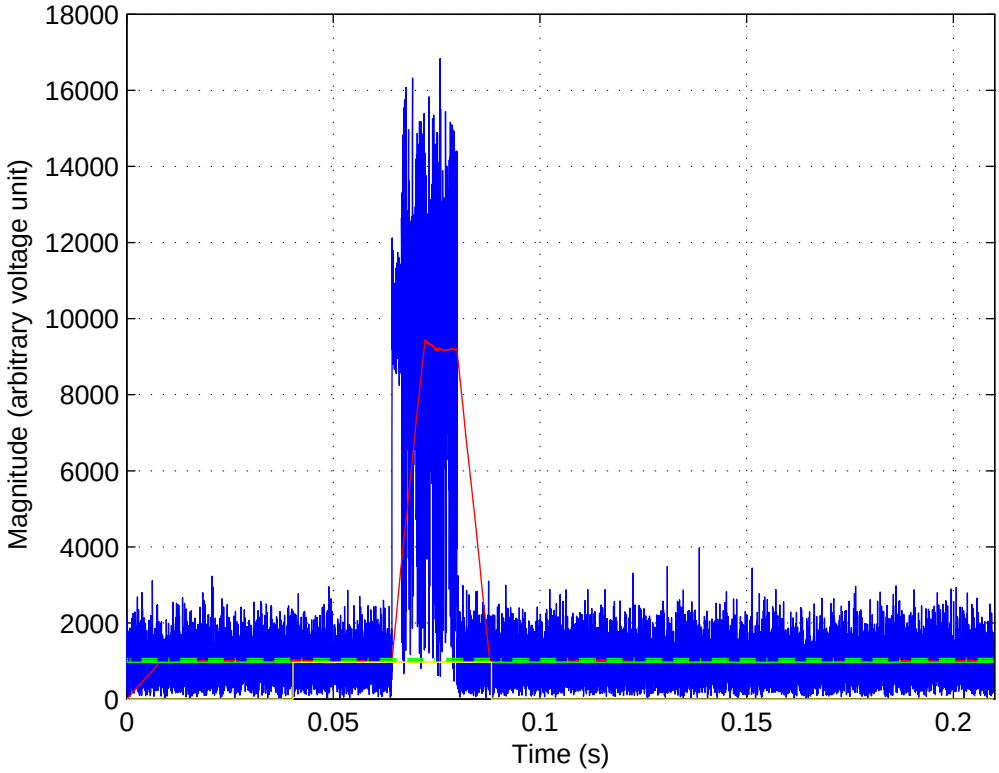

Figure 5.9: Magnitude of received data file and envelope of detector

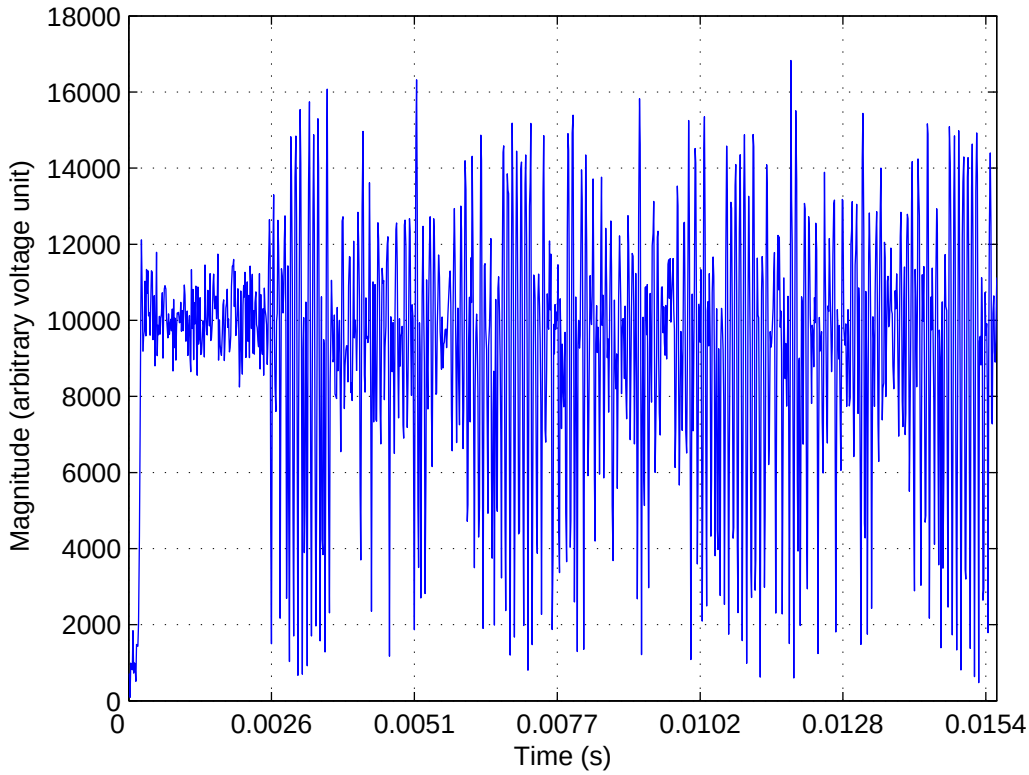

Figure 5.10: Detected burst

5.5.2 Signal Estimation and Demodulation

Figure 5.11 shows the I-Q diagram of the baseband signal sampled at 78.125 kSPS. In order to estimate the carrier center frequency, a FFT of the tone burst is computed. Figure 5.12 shows the FFT of the tone burst (here tone burst is usually about first 200 samples). The peak of the FFT provides a rough estimation of the center frequency. Next, a brute force search is conducted over the range of few FFT bins around the center frequency found from the FFT. In this case, 3 FFT bins is used. The peak of the maximum likelihood estimator (MLE) is the refined center frequency. Figure

5.13 shows the result of this MLE by brute force search. Once the center frequency is determined, the burst is down-converted to baseband. Figure 5.14 shows the FFT of the baseband signal to verify that the center frequency has moved from passband to baseband. Figure 5.15 and 5.16 shows the I-Q diagram of baseband data and phase angle plot of the baseband data after downconversion. The variation of carrier phase over the burst is assumed as static (or at least insignificant). This is a valid assumption in this case; had this assumption been wrong, the demodulation of symbols would not work, contrary to the results shown later.

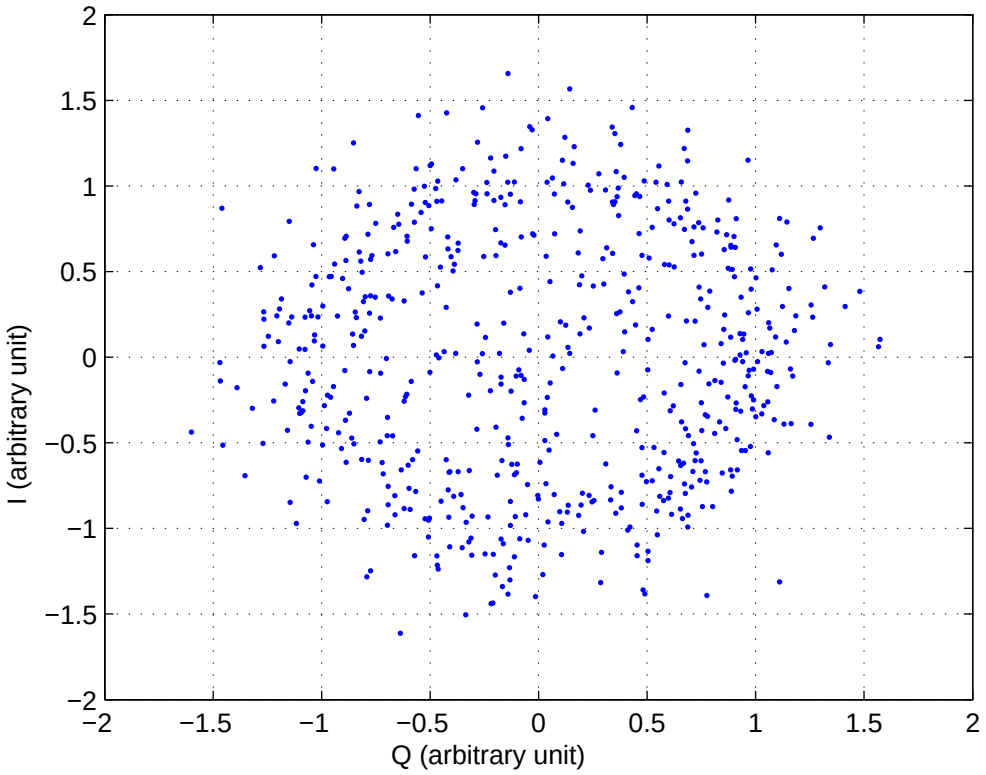

Figure 5.11: Bandpass signal in signal space sampled at 78.125 kSPS

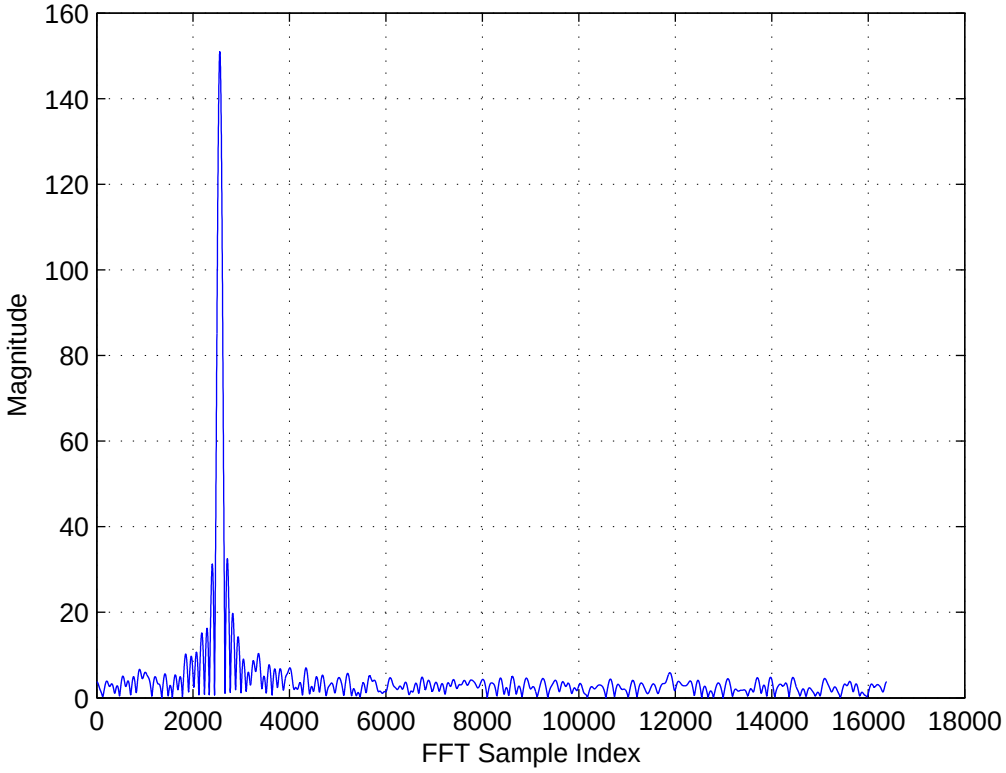

Figure 5.12: FFT of bandpass tone burst to find out center frequency; $\hat{f}_c = 1.2187 \times 10^4$ Hz.

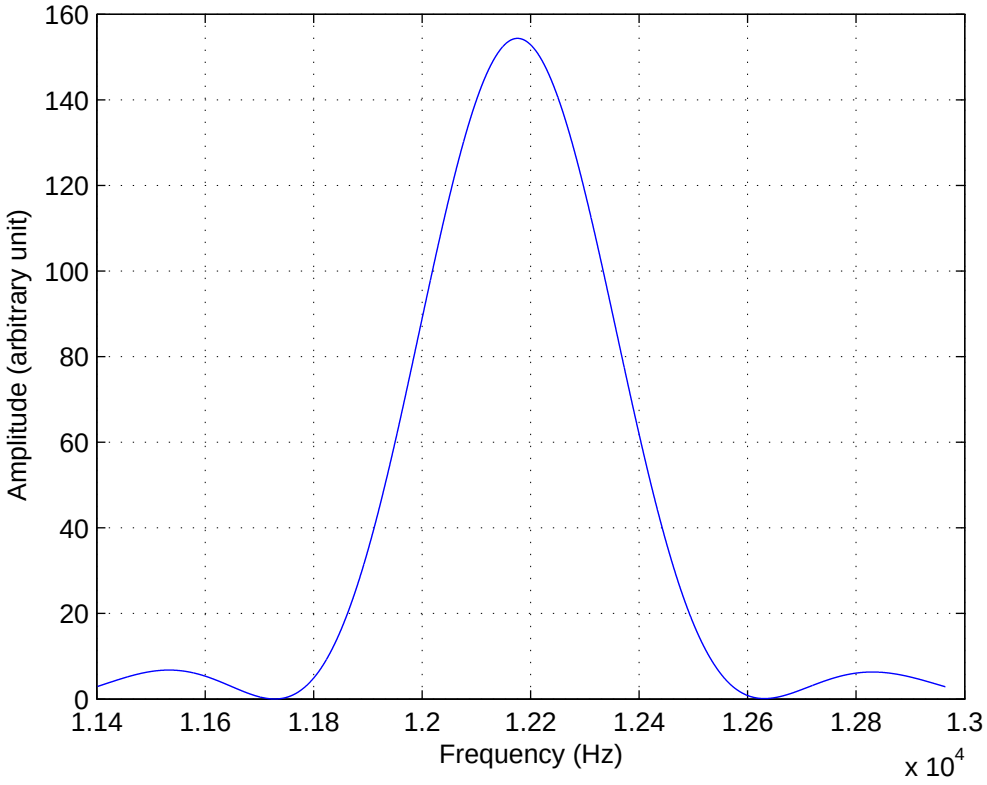

Figure 5.13: ML Estimation to find out the center frequency; $\hat{f}_c = 1.2184 \times 10^4$ Hz.

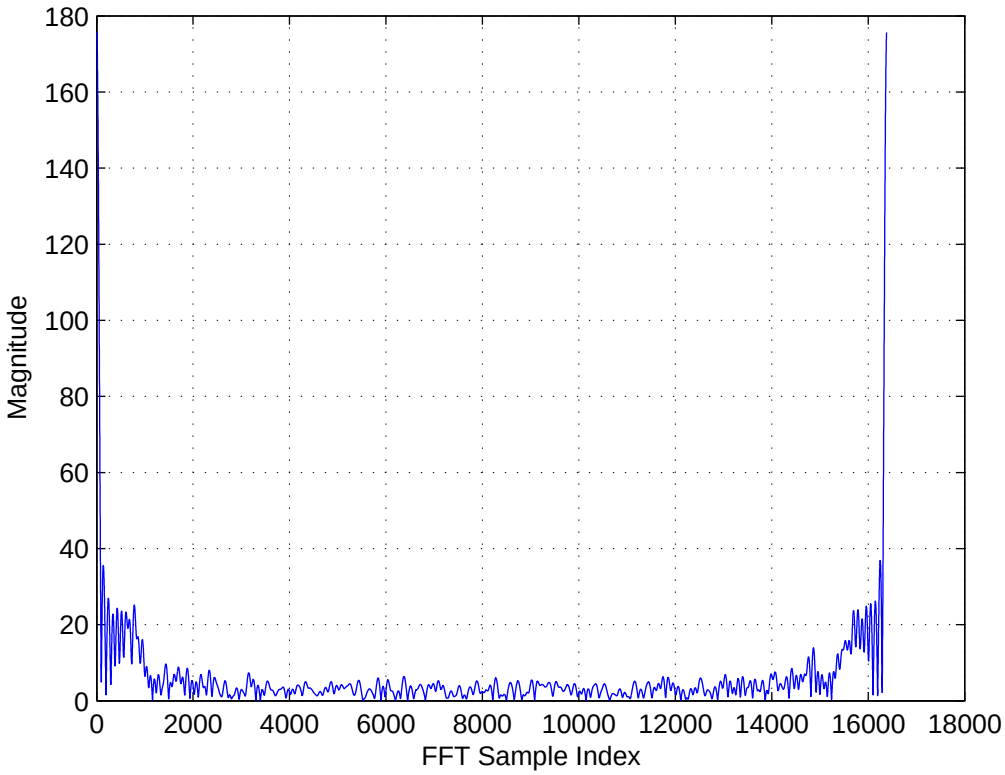

Figure 5.14: FFT of tone burst, after downconverting, shows that downconversion was performed properly

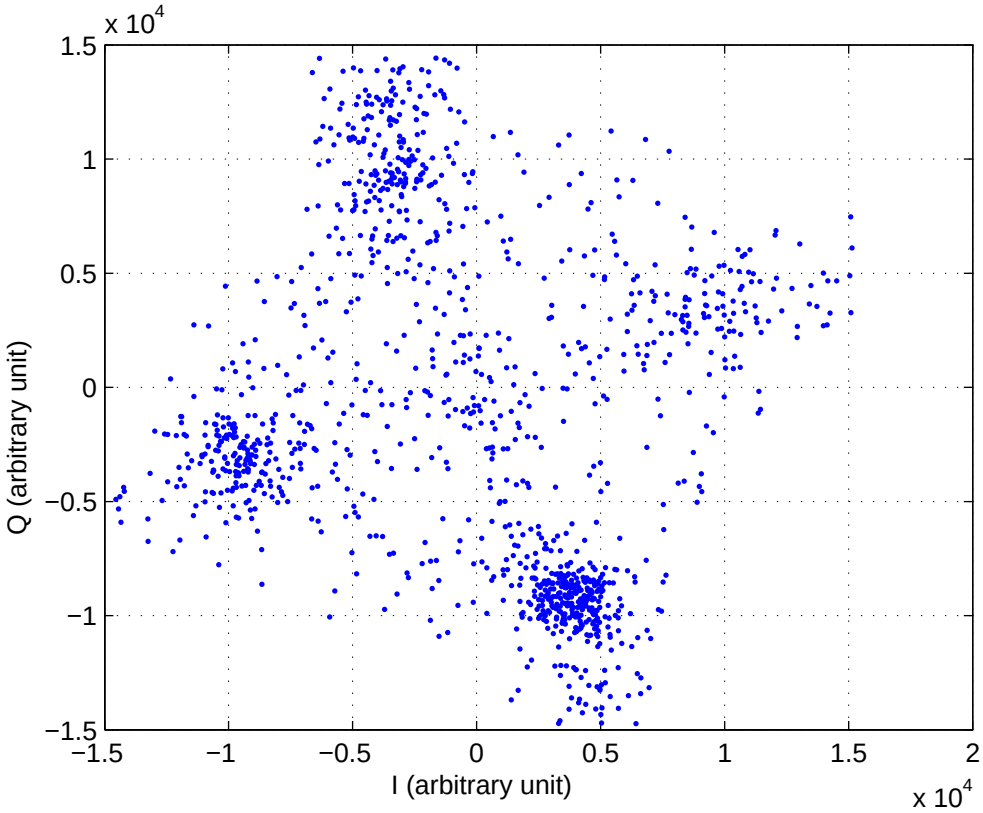

Figure 5.15: I-Q Diagram of baseband data burst, after downconverting, sampled at 78.125 kSPS

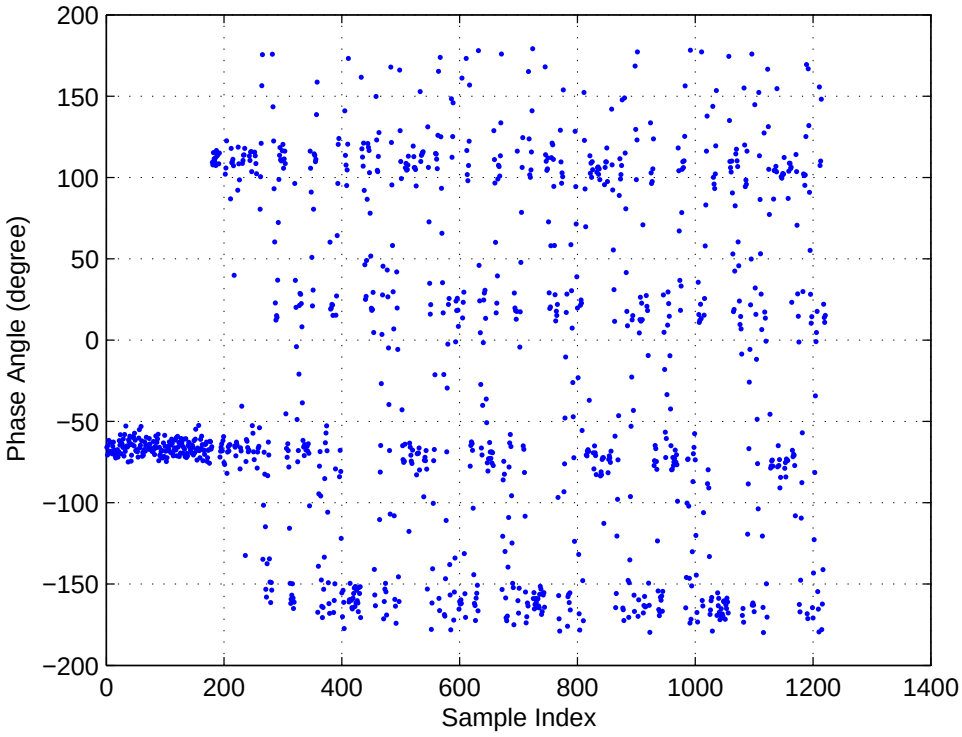

Figure 5.16: Phase plot of baseband signal sampled at 78.125 kSPS

The next step is to determine the symbol timing. Figure 5.17 shows the output of the symbol recovery filter where the uppermost line represents symbol timing with the highest energy. Once the symbol timing value is estimated, the baseband signal is adjusted for symbol timing delay. It is then converted to a signal with 100 kSPS (4 samples/symbol) from 78.125 kSPS data using a filter that uses Nyquist's sampling theorem. Figure 5.18 shows baseband signal resampled 100 kSPS. Figure 5.19 shows the signal decimated to symbols with symbol rate of 25 kSy/s. Figure 5.20 shows the phase angle plot of the signal.

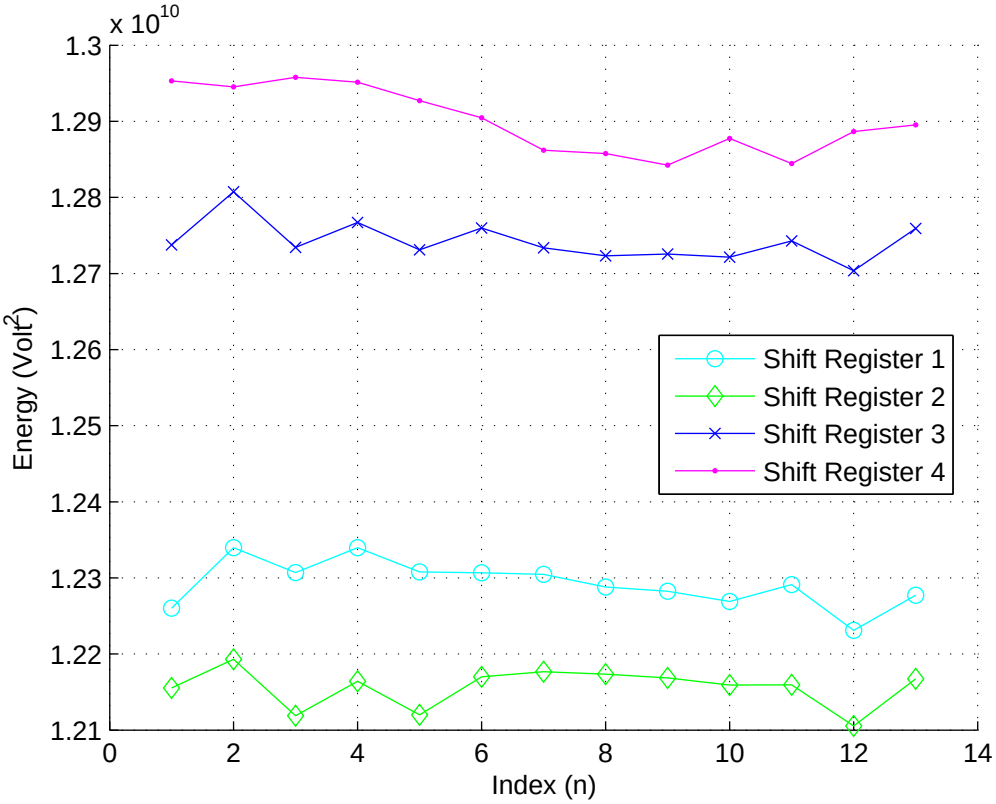

Figure 5.17: Symbol timing recovery process

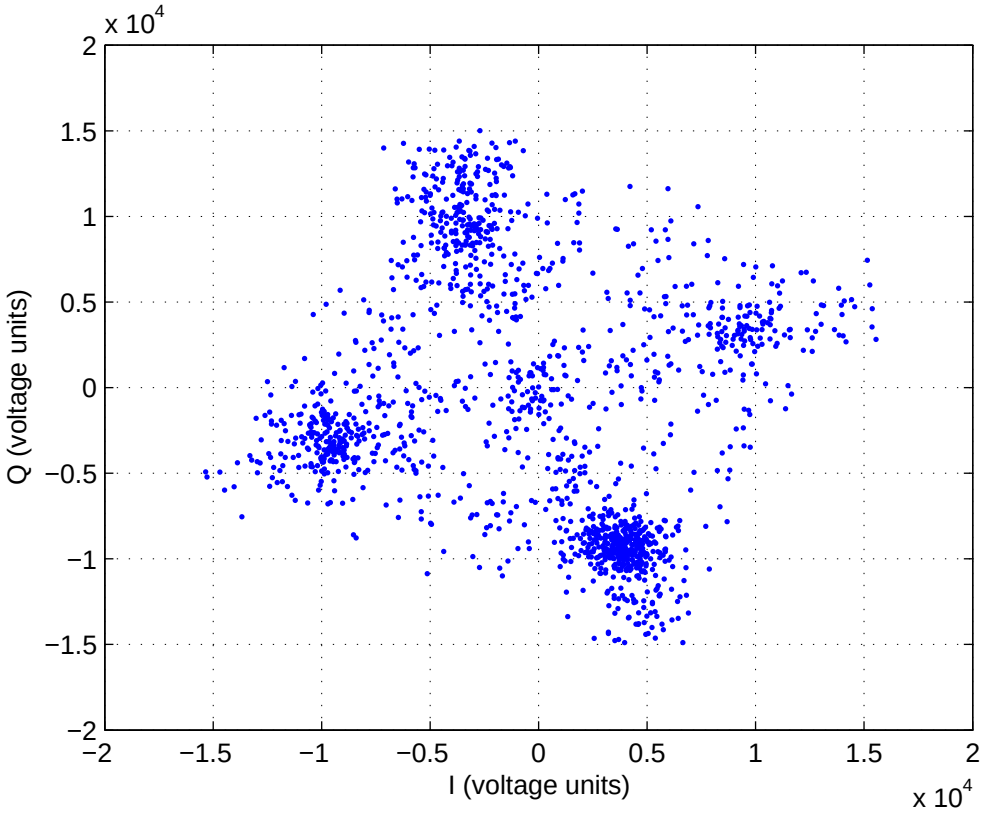

Figure 5.18: I-Q diagram of baseband data burst resampled at 100 kSPS

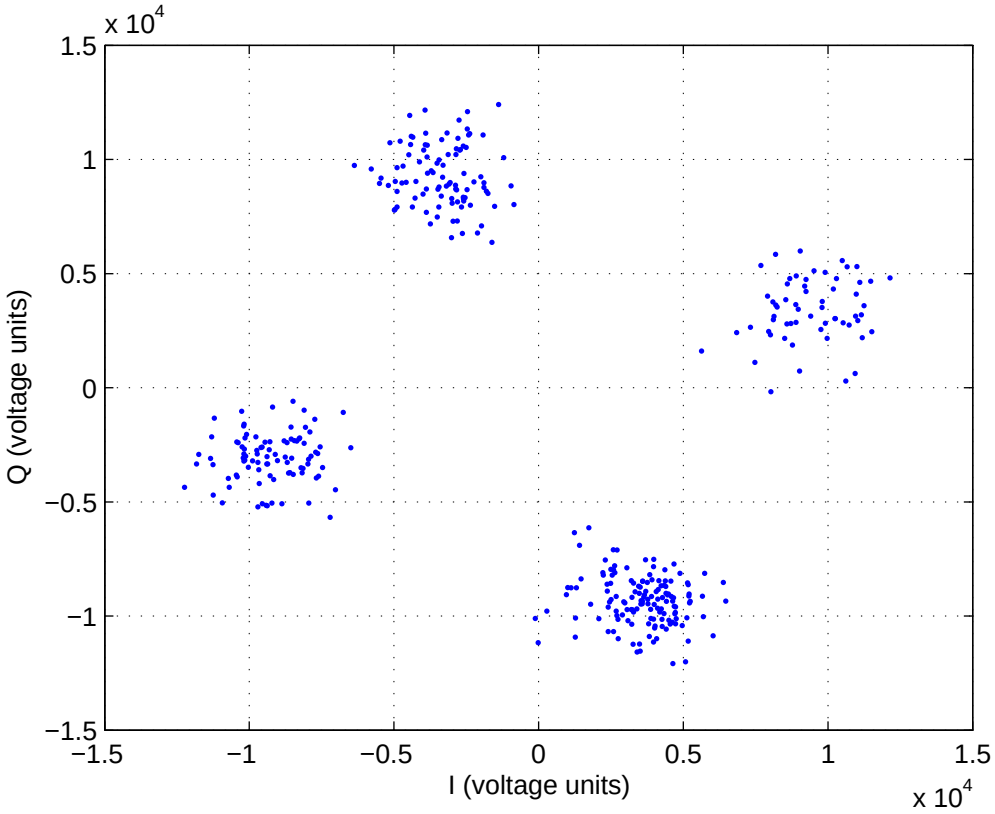

Figure 5.19: I-Q diagram of baseband decimated burst to 25 kSy/s

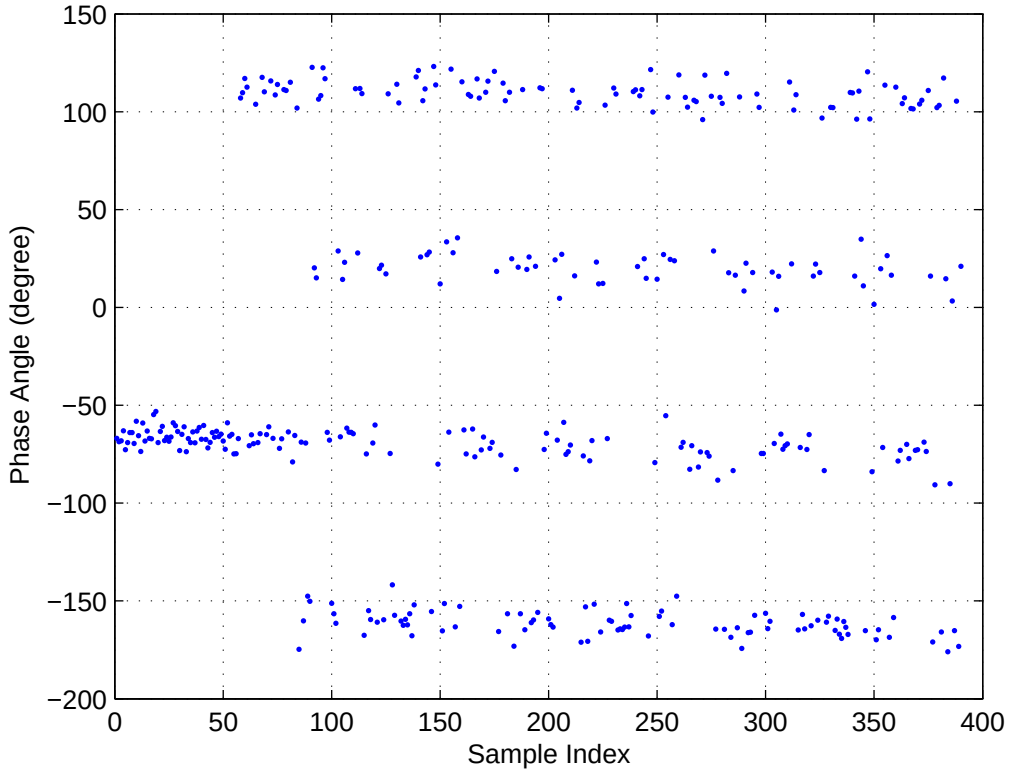

Figure 5.20: Phase angle plot of baseband signal sampled at 25 kSy/s

Once the appropriate symbols are determined, hard liming is performed so that the symbols fall in the unit circle. Figure 5.22 represents the I-Q diagram of the baseband hard limited data decimated to 25 kSy/s. Figure 5.21 shows the correlation between the unique word and the baseband signal. Phase rotation introduced during propagation can be found from this correlation. The phase angle of the peak of correlation is that phase rotation factor. Once the phase rotation factor is determined, the signal can be rotated to find out the actual orientation of the constellation diagram. Figure 5.23 shows the I-Q diagram of hard-limited and phase rotated baseband signal.

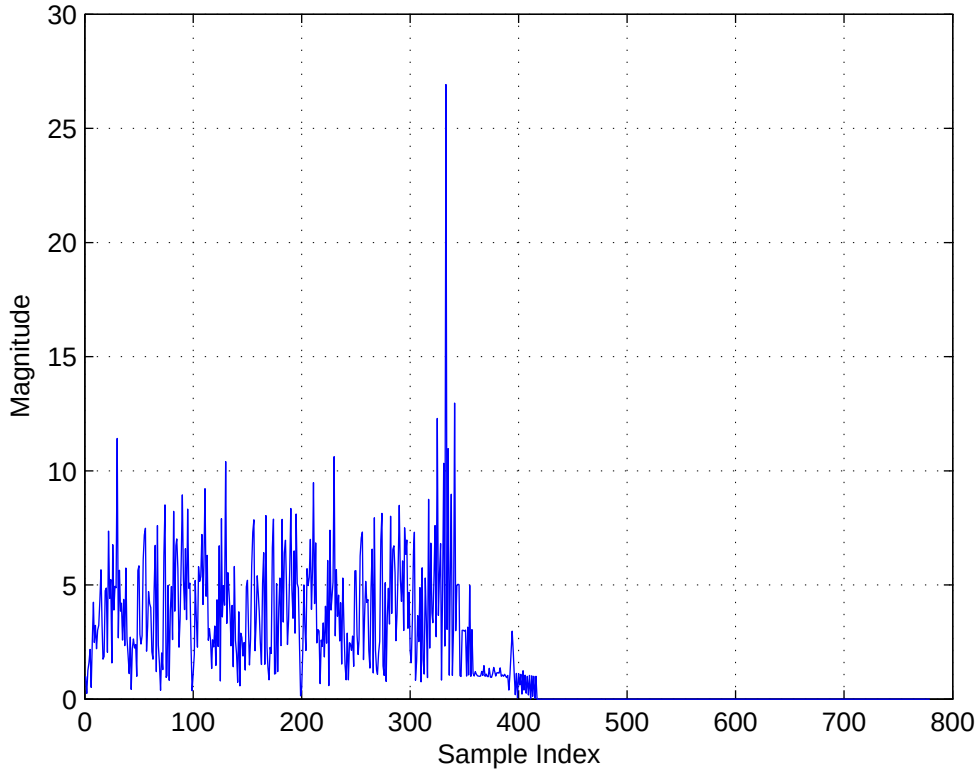

Figure 5.21: Correlation between unique word and baseband signal

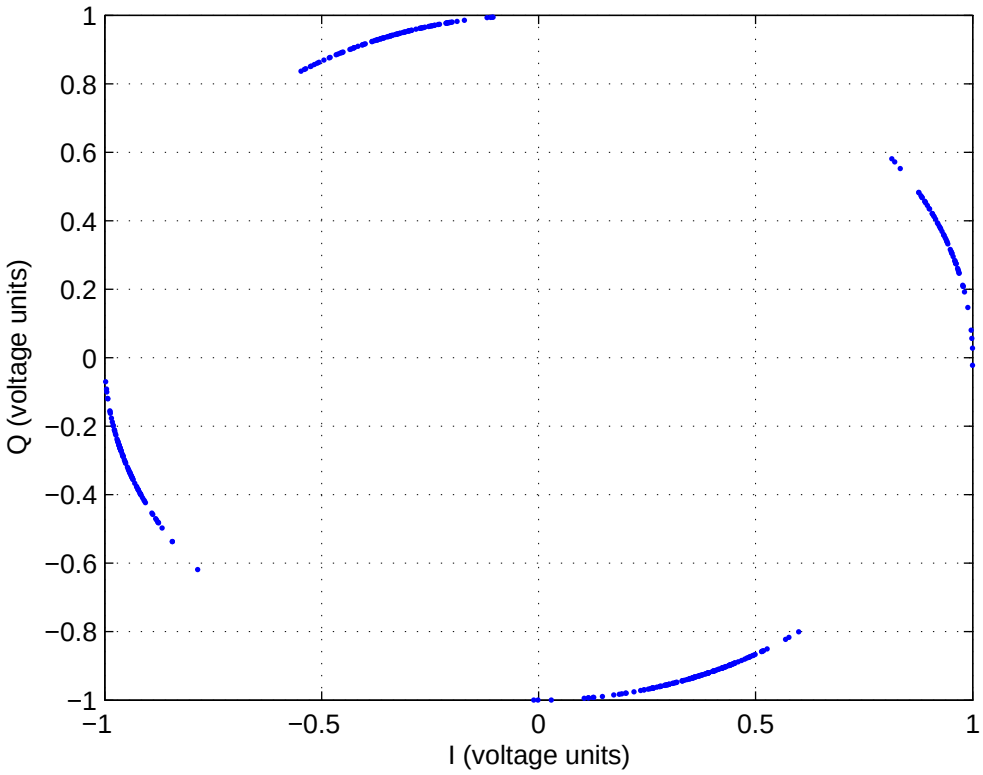

Figure 5.22: I-Q diagram of baseband decimated hard-limited burst to 25 kSy/s

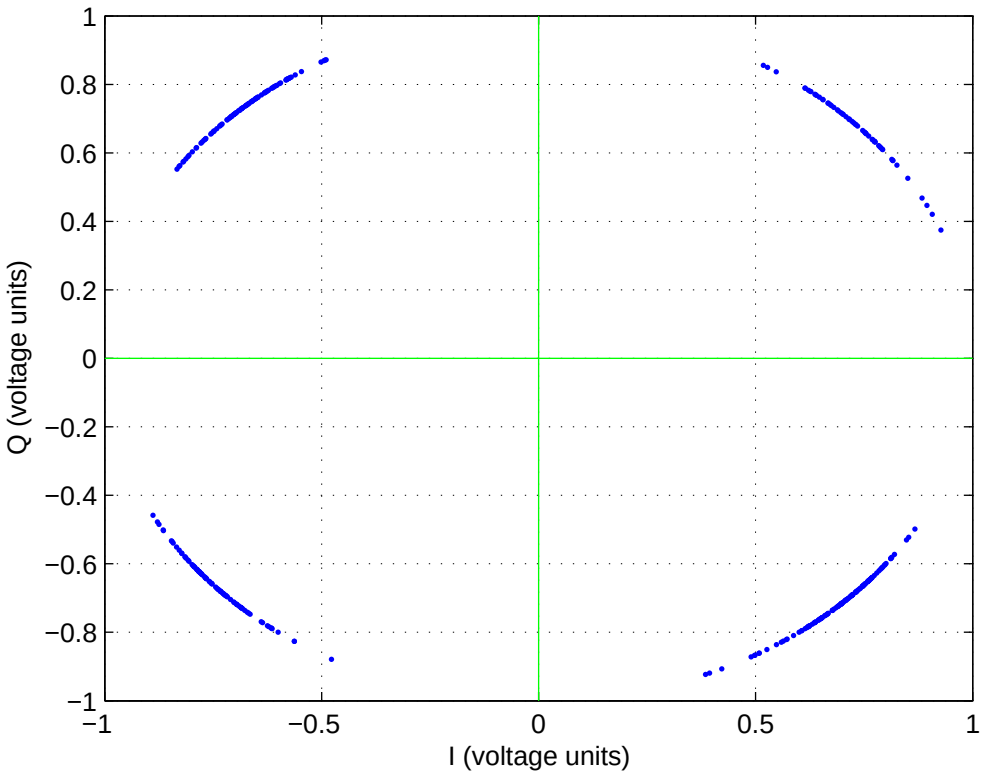

Figure 5.23: I-Q diagram of hard-limited and phase rotated baseband signal

5.5.3 Signal Remodulation and Synthesis

Figure 5.24 shows the I-Q constellation diagram of the re-modulated signal. It is phase shifted exactly the same amount found during demodulation. The remodulated symbols have a rate of 25 kSy/s which is then upsampled and pulse shaped to 100 kSPS by using zero insertion and pulse-shaping process. Figure 5.25, 5.26 and 5.27 respectively shows root-raised cosine function samples (with sampling rate of 100 kSPS and symbol rate of 25 kSy/s, which is used as coefficient of pulse shaping filter), zero inserted synthesized baseband signal, and pulse shaped and upsampled

synthesized baseband signal sampled at 100 kSPS. Both 5.28 and 5.29 show I-Q diagram of the 'pulse shaped and upsampled' synthesized baseband signal sampled at 100 kSPS.

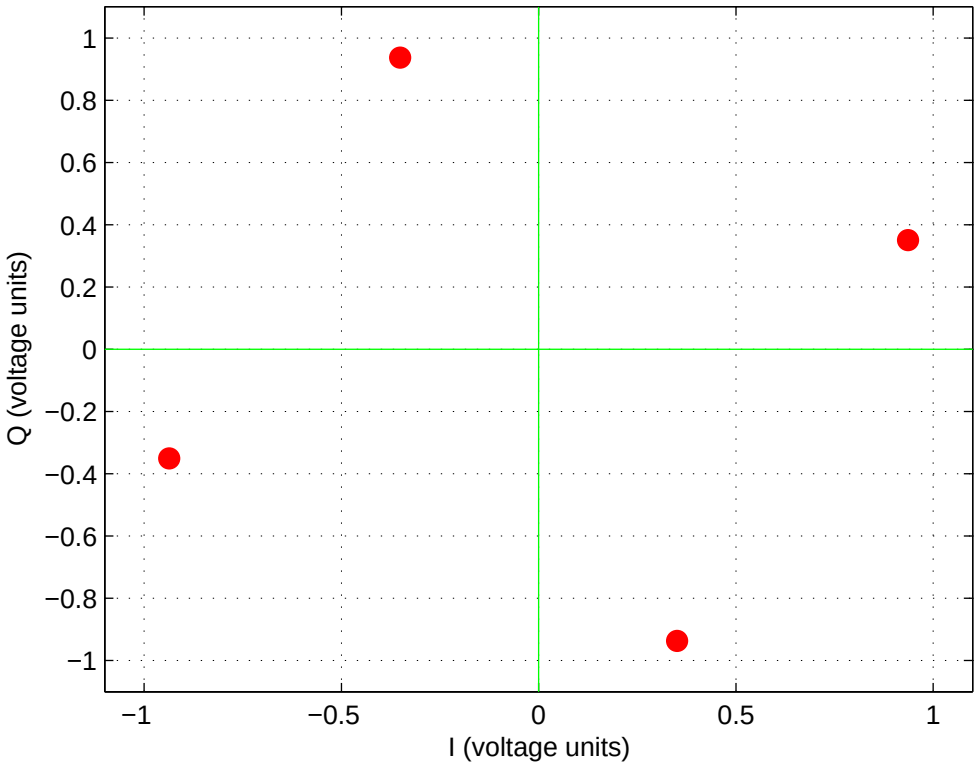

Figure 5.24: I-Q diagram of remodulated baseband signal at 25 kSy/s

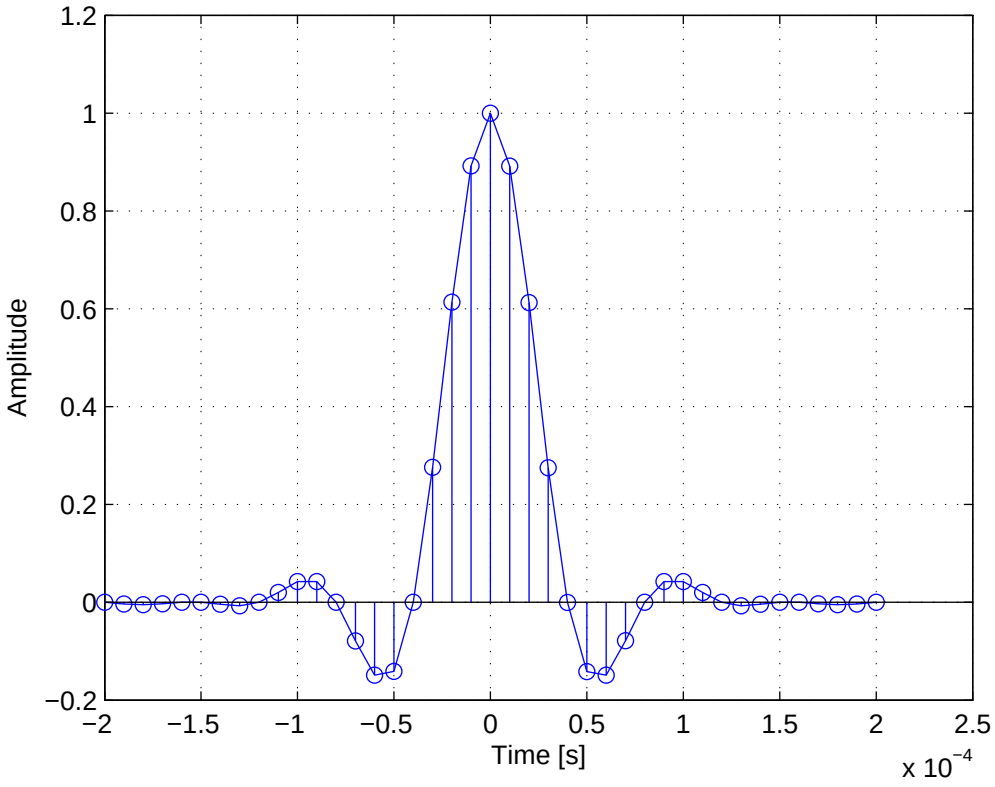

Figure 5.25: Raised cosine filter for 100 kSPS, 25 kSy/s with 41 taps

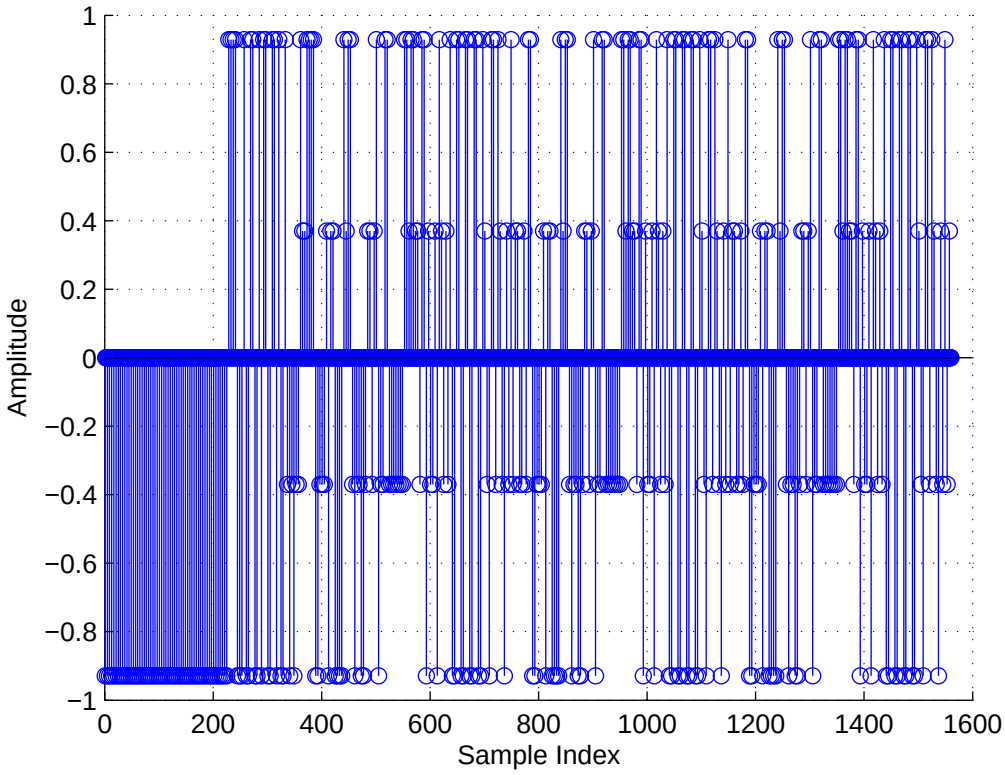

Figure 5.26: Zero inserted synthesized baseband signal (at 100 kSPS)

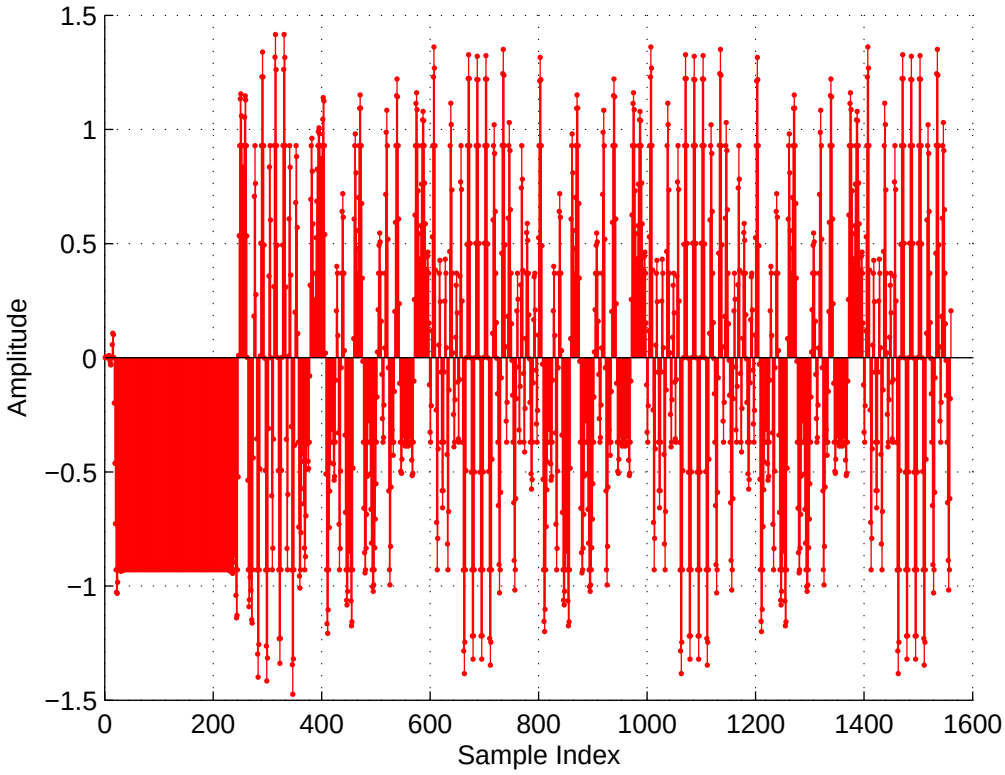

Figure 5.27: Pulse shaped and upsampled signal (at 100 kSPS)

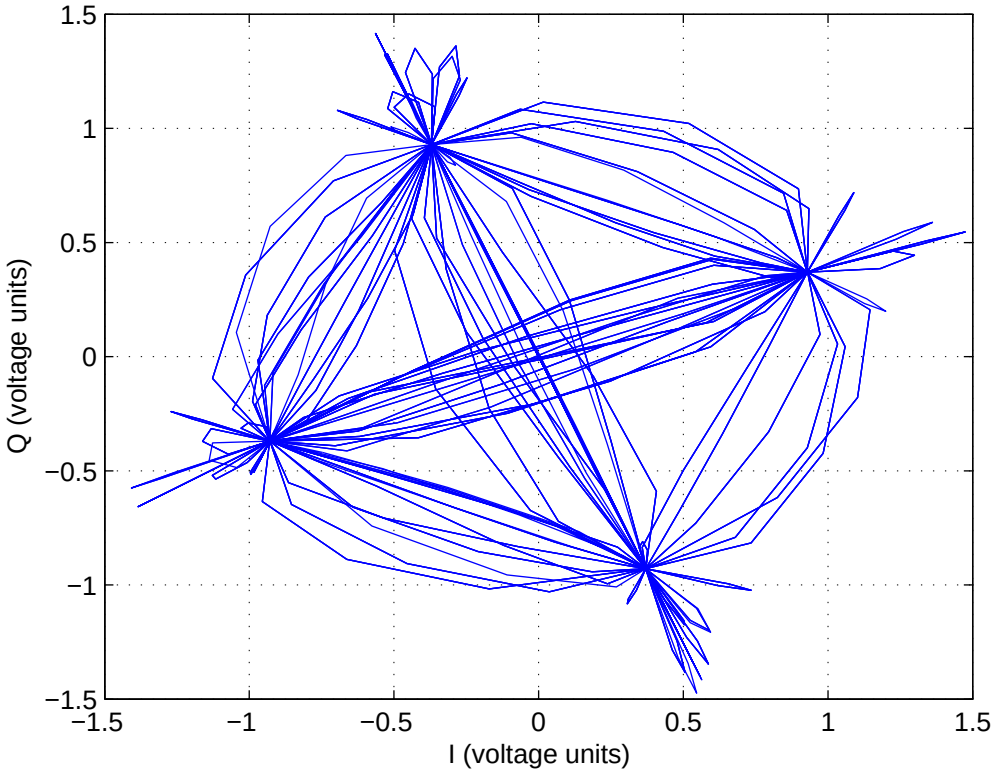

Figure 5.28: I-Q diagram of pulse shaped and upsampled signal sampled at 100 kSPS

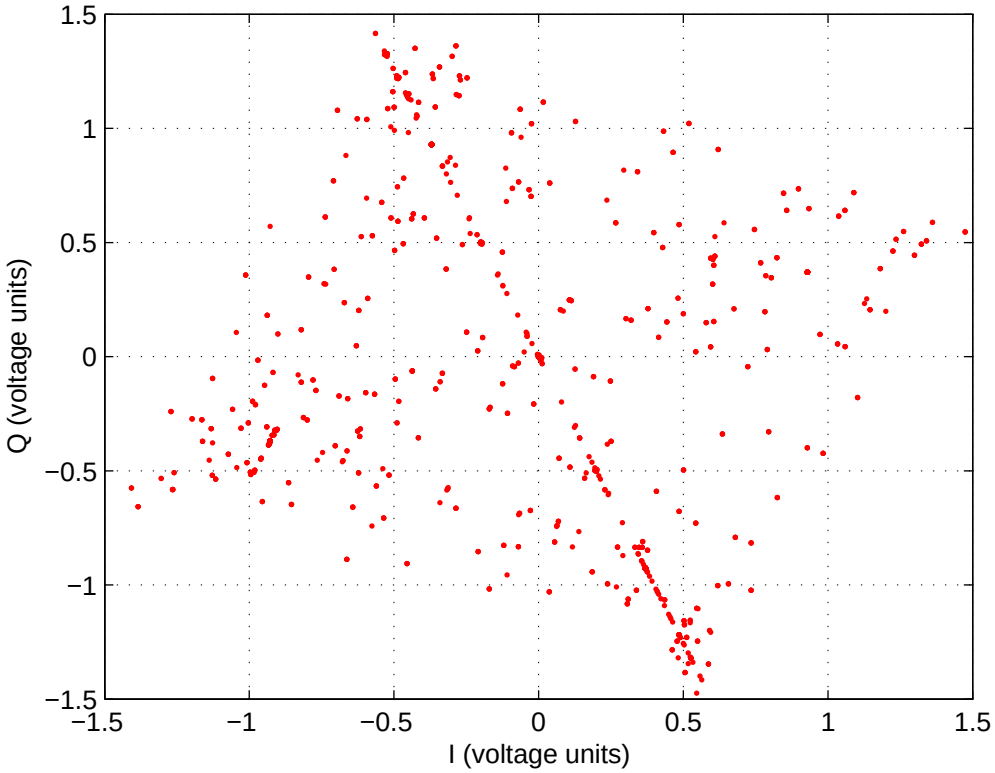

Figure 5.29: Synthesized baseband signal resampled at 100 kSPS

The next step is to resample the signal at of 78.125 kSPS (from 100 kSPS) by using Equation (4.20). Figure 5.30 shows the reconstructed synthesized baseband signal re-sampled at 78.125 kSPS.

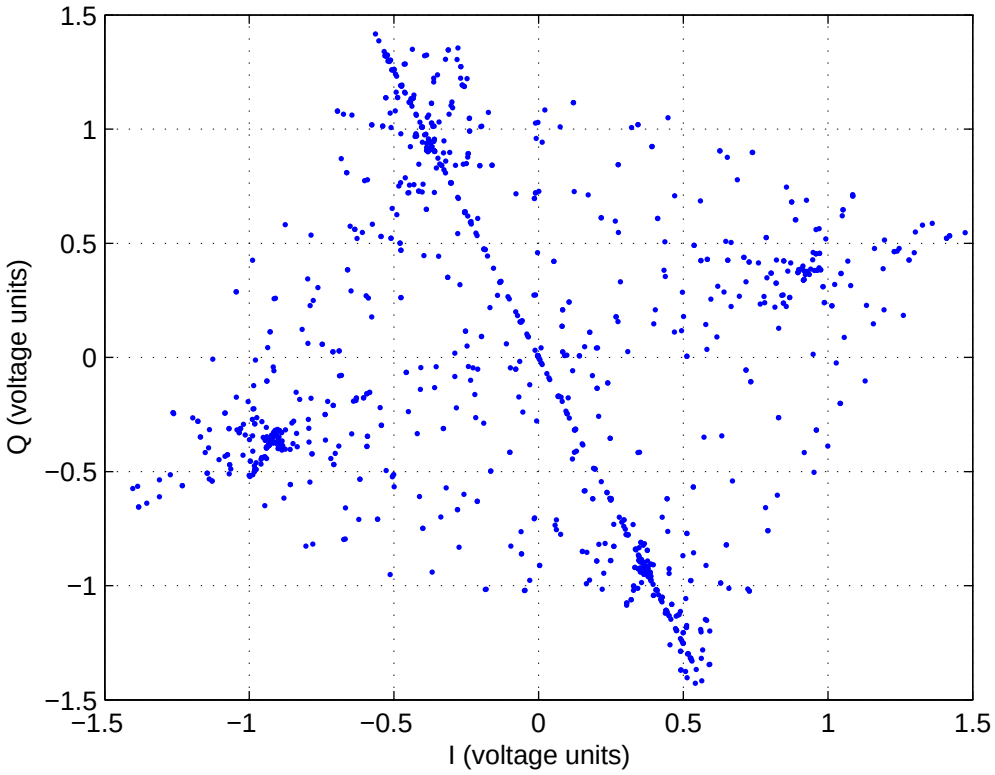

Figure 5.30: Synthesized baseband signal resampled at 78.125 kSPS

Figure 5.31 shows the correlation between original and synthesized signal. The peak of the correlation represents the complex magnitude value of the original signal. The cumulative delay associated with the filters used through the process can also be determined from this correlation which is used later to align the original and synthesized signal in order to subtract coherently.

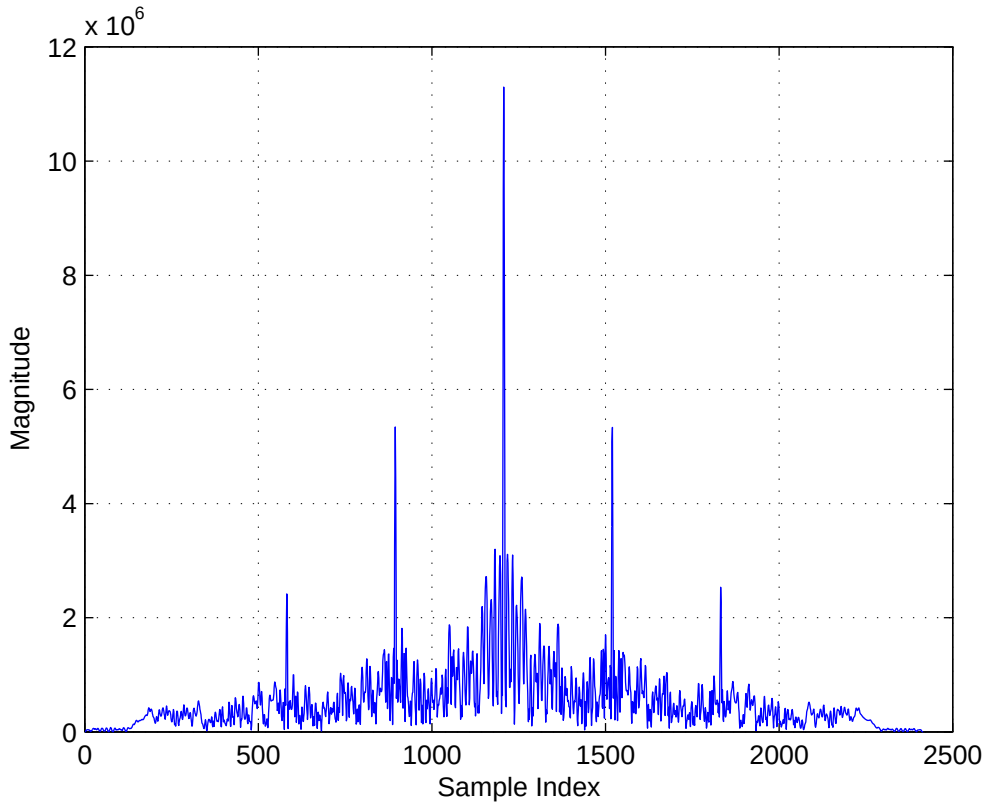

Figure 5.31: Correlation of original and synthesized signal to find complex magnitude

5.5.4 Cancelation

In this section, the canceling performance of the proposed algorithm is observed for a signal that has 10 dB SNR. Both time domain and frequency domain results are presented here. Figure 5.33 and 5.32 shows respectively frequency domain and time domain representation of signal for 10 dB SNR. It can be observed that the proposed interference mitigation scheme achieves 8 dB of suppression for 10 dB SNR. Figure 5.34 shows the before and after integrated spectrum for this signal.

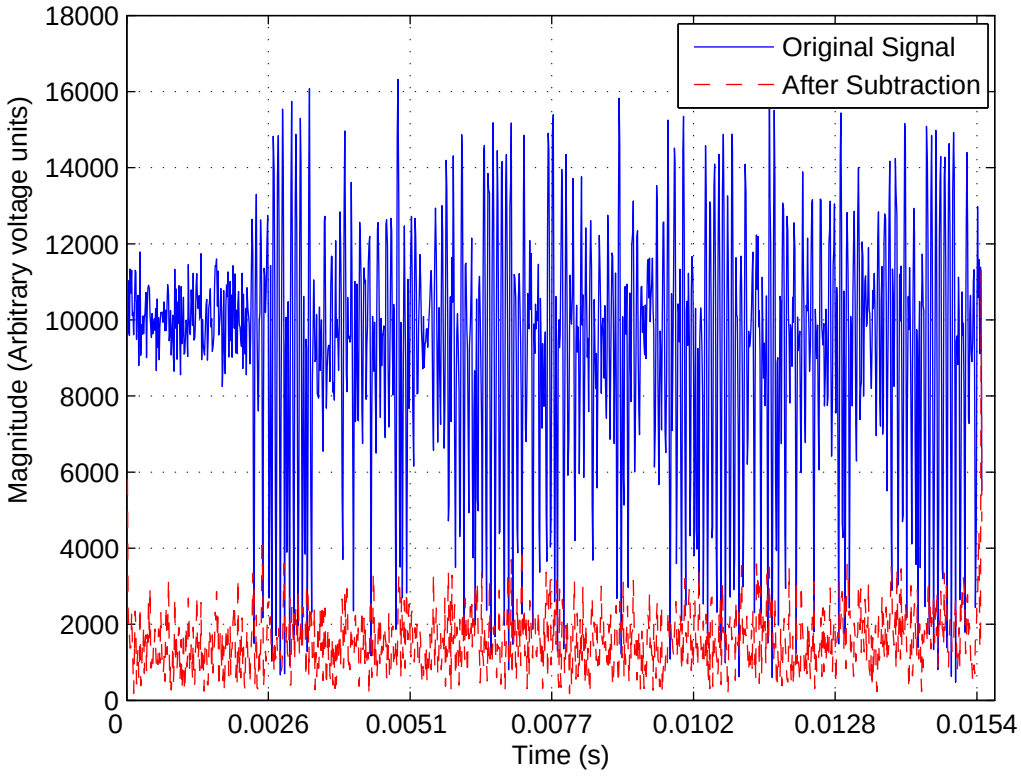

Figure 5.32: Time domain representation of signal for SNR = 10 dB

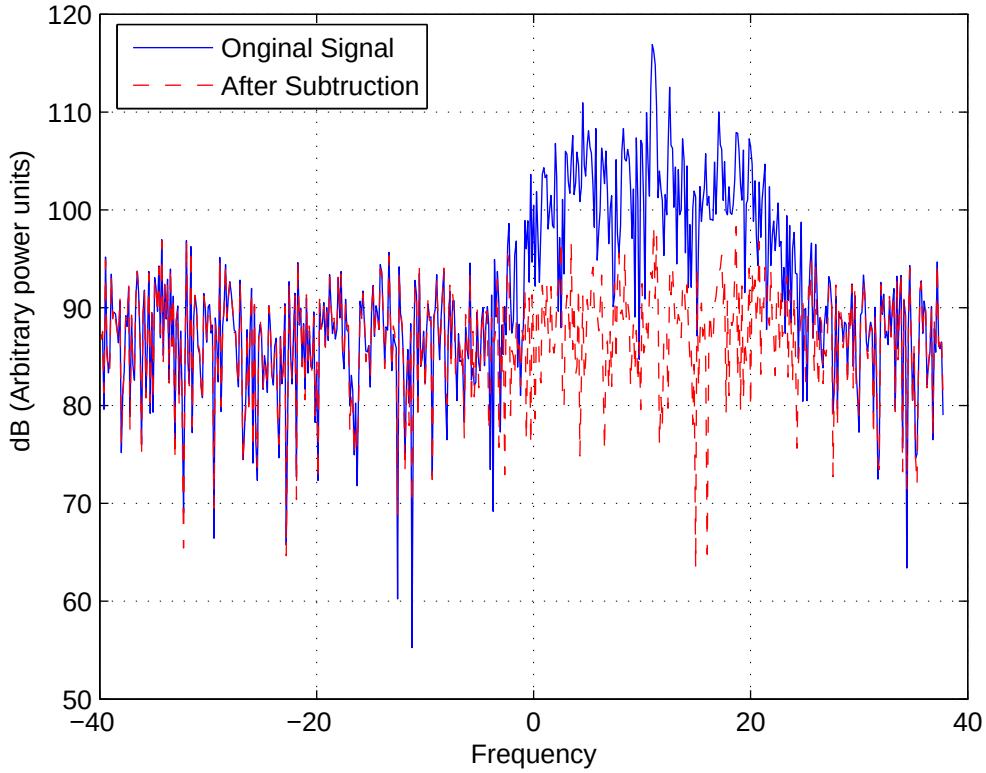

Figure 5.33: Frequency domain representation of signal for SNR = 10 dB

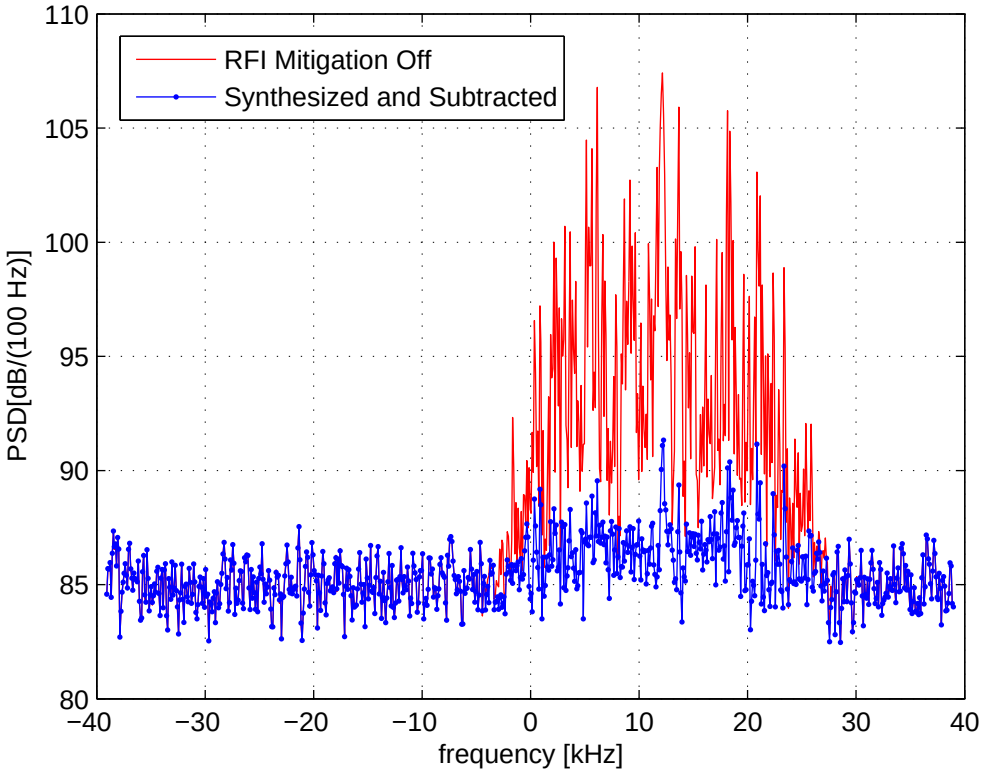

Figure 5.34: Frequency domain representation of signal for SNR = 10 dB

5.6 Performance Comparison Between Detect/Blank Vs Detect/Cancel

In this section, the proposed algorithm (Detect/Cancel) is compared with a Detect/Blank algorithm. Figure 5.35 shows the integrated spectrum of the original signal, time blanked signal, and synthesized and subtracted signal. In this simulation, a signal with 30 dB SNR is used. It can be observed that time blanking achieves 29 dB while the "synthesized and subtracted" signal achieves about 15 dB suppression.

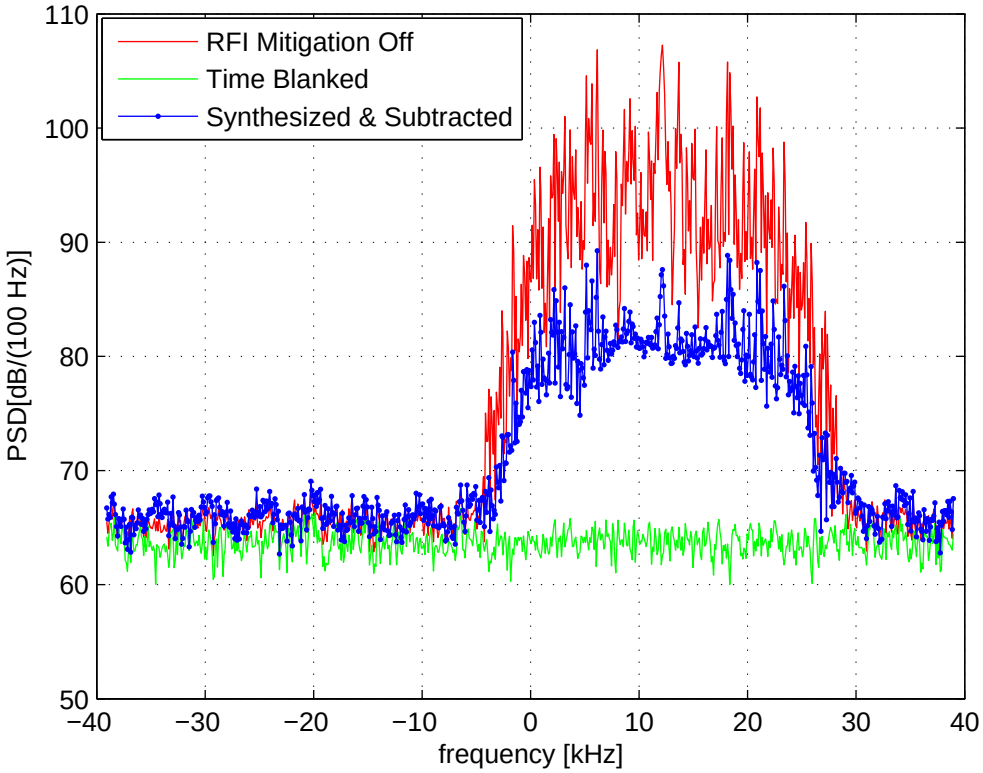

Figure 5.35: Performance comparison between Detect/Blank Vs Detect/Cancel: before and after integrated spectrum

Figure 5.36 shows a performance comparison between Detect/Blank and Detect/Cancel, in terms of suppression (dB) vs. SNR. In can be seen from Figure 5.36 that the amount of suppression increases with the increase of SNR. It is clear that the time-blanking outperforms "synthesization and subtraction" method regardless of the signal SNR. However, the difference increases with the increase of SNR.

It is not surprising that the time blanking always outperforms "synthesize and subtract" method regardless of the signal SNR. Time blanking method works by zeroing all the data whereas "synthesize and subtract" method tries to recreate interfering burst and eliminate it. One can achieve maximum suppression by zeroing everything within the burst period. However, one significant drawback of time blanking is that both interfering signal and desired data is lost forever in this process. Thus, it can be hazardous in many sensitive cases.

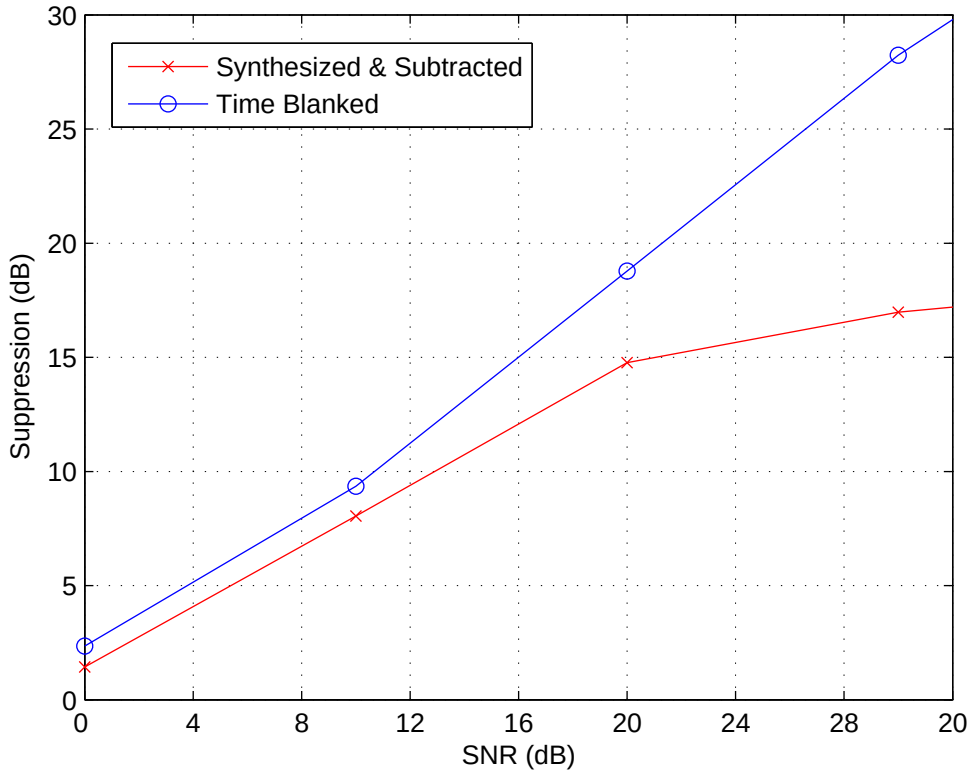

Figure 5.36: Performance comparison between Detect/Blank Vs Detect/Cancel: suppression (dB) vs. SNR

Chapter 6

Algorithm Validation on Real Data

In this chapter, the proposed algorithm is validated by using real data. In Section 6.1, the Argus instrument, which is used to capture real data, is presented. In Section 6.2, a description of the real dataset is presented. In Section 6.3, a comparison of performance between two methods: (1) Detect/Blank, and (2) Detect/Cancel, is presented.

6.1 Argus Radio Telescope

The data used in this thesis is obtained from the Argus radio telescope. Argus is an experimental omni-directional radio telescope developed by a group of scientists, graduate and undergraduate students of the Ohio State University [26]. Argus aims to detect the L-Band signals coming from almost all directions of the sky by using a large numbers of low gain (broadbeam) elements to achieve sensitivity over the entire sky. Figure 6.1 shows the Argus antenna array.

There are total 36 elements array in Argus of which 24 are instrumented. It is capable of tuning from 1200 to 1700 MHz. It digitizes at 20 MSPS complex (14 MHz BW); which is then processed to 78.125 kSPS complex [27].

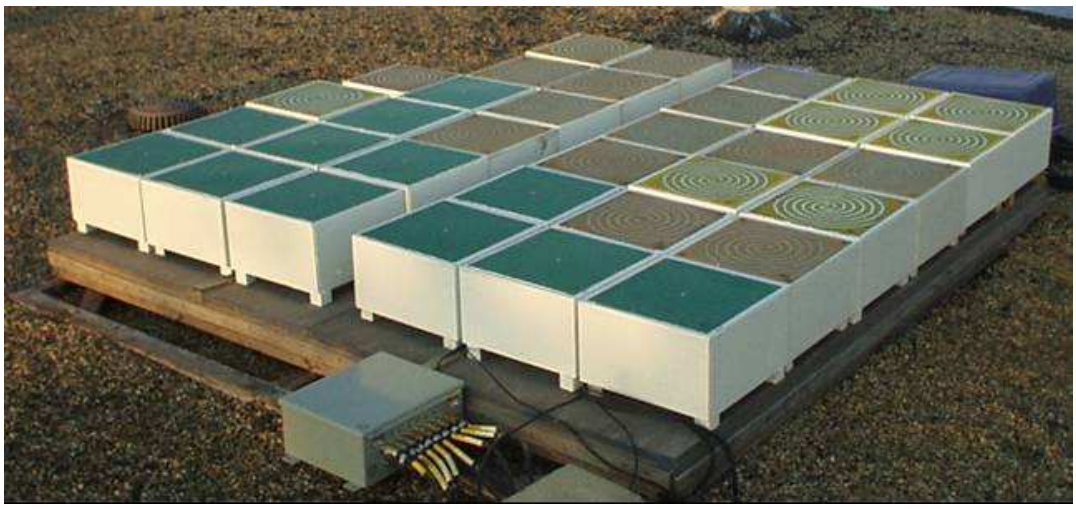

Figure 6.1: Argus antenna array

6.2 Description of Real Dataset

In this section, details of the real data captured from Iridium by Argus is presented. Figure 6.2 shows a time domain magnitude plot (in dB) of the data collected for a single element in the Argus array. Several characteristics are immediately apparent: each burst has an unmodulated code word (CW) tone burst, unique word (UW) and information data.

Figure 6.2 shows a few Iridium bursts captured using Argus. Figure 6.3 is a zoomed plot of Figure 6.2, focusing on the first, larger burst. From Figure 6.3, it can be seen that the preamble length is approximately 200 samples, or 2.56 ms with sampling rate of 78.125 kSPS. Over all the bursts analyzed, the average preamble length is found to be 195 samples, or 2.5 ms.

Whereas each Iridium burst preamble has approximately same length, the total length of the bursts are not the same. By comparing the time between bursts, shown

in Figure 6.2, it was verified that the time between each burst is 90 ms [28].

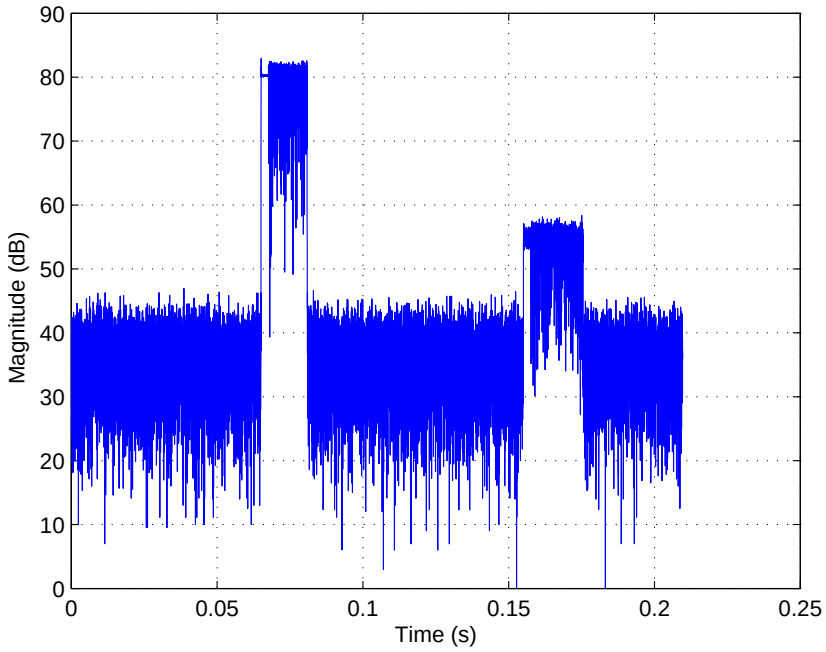

Figure 6.2: Time domain magnitude plot of some observed bursts

The center frequency of each burst was estimated by maximum likelihood estimator (MLE) with brute force search. The complex baseband representation of the burst is then frequency shifted, centering the spectrum of each burst at zero. Figure 6.4 shows the time domain phase angle plot of the burst shown in Figure 6.3.

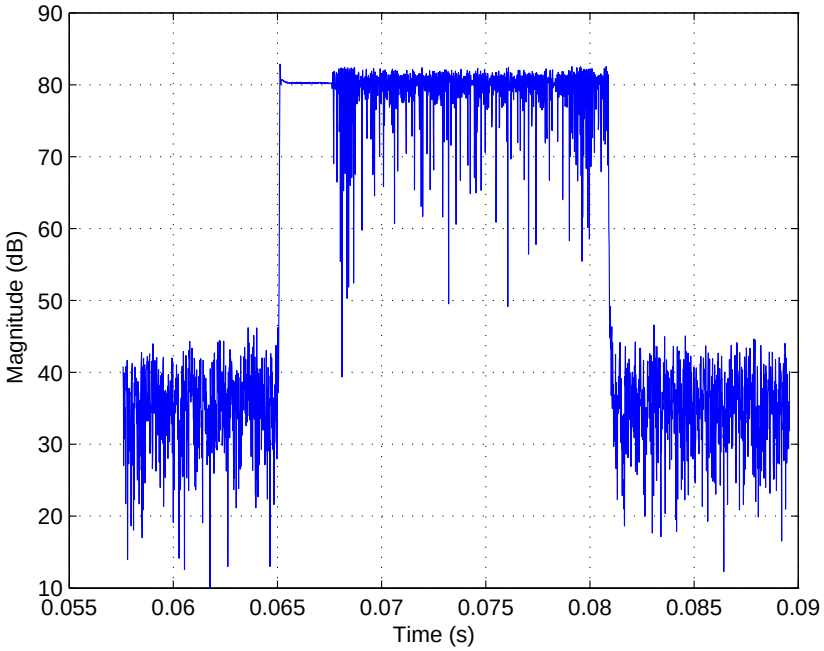

Figure 6.3: Zoomed version, showing the first, larger pulse's CW preamble, a unique word, and modulated data

Figure 6.4 clearly shows the CW preamble followed by a BPSK-modulated unique word and QPSK-modulated data. Figure 6.5 shows the same information for the second, and strongest, burst. Although the burst shown in Figure 6.5 is less than half the length of the burst shown in Figure 6.4, it is again clear that the burst is composed of a CW preamble followed by a set of BPSK unique word and QPSK data. The comparison of Figure 6.4 and Figure 6.5 yield a strong correlation at the beginning of the dataset, indicating the unique word. Figure 6.6 shows the phase angle plot of the unique word.

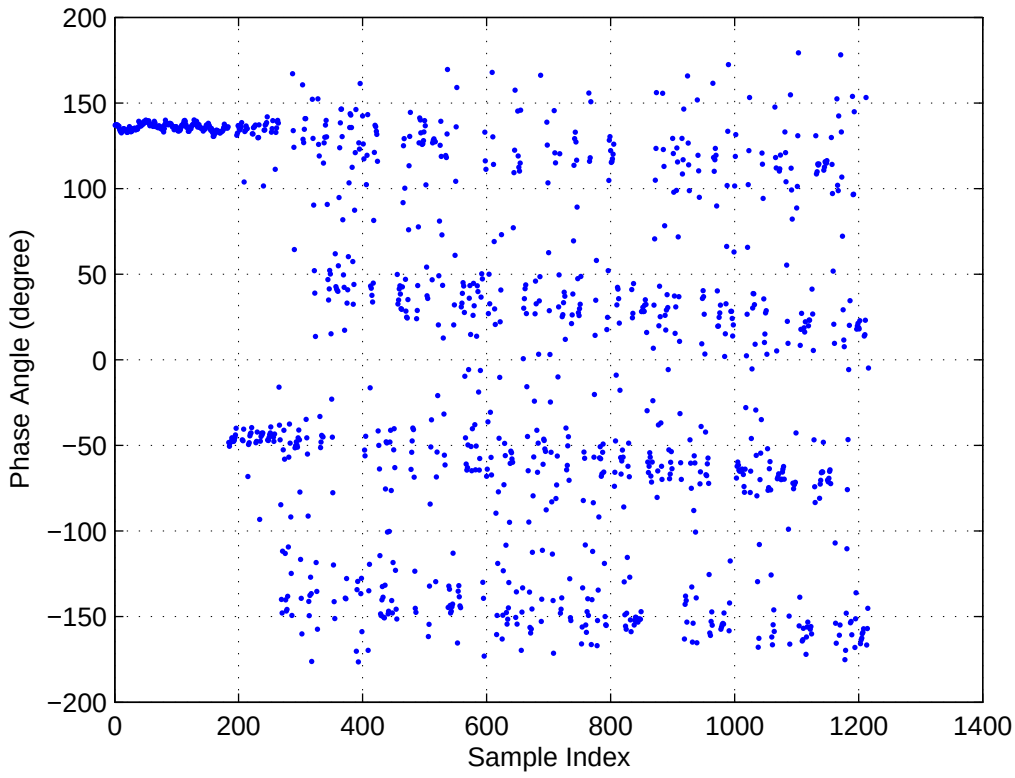

Figure 6.4: Phase angle plot of the burst 1 showing the CW preamble, BPSK unique word, and QPSK data.

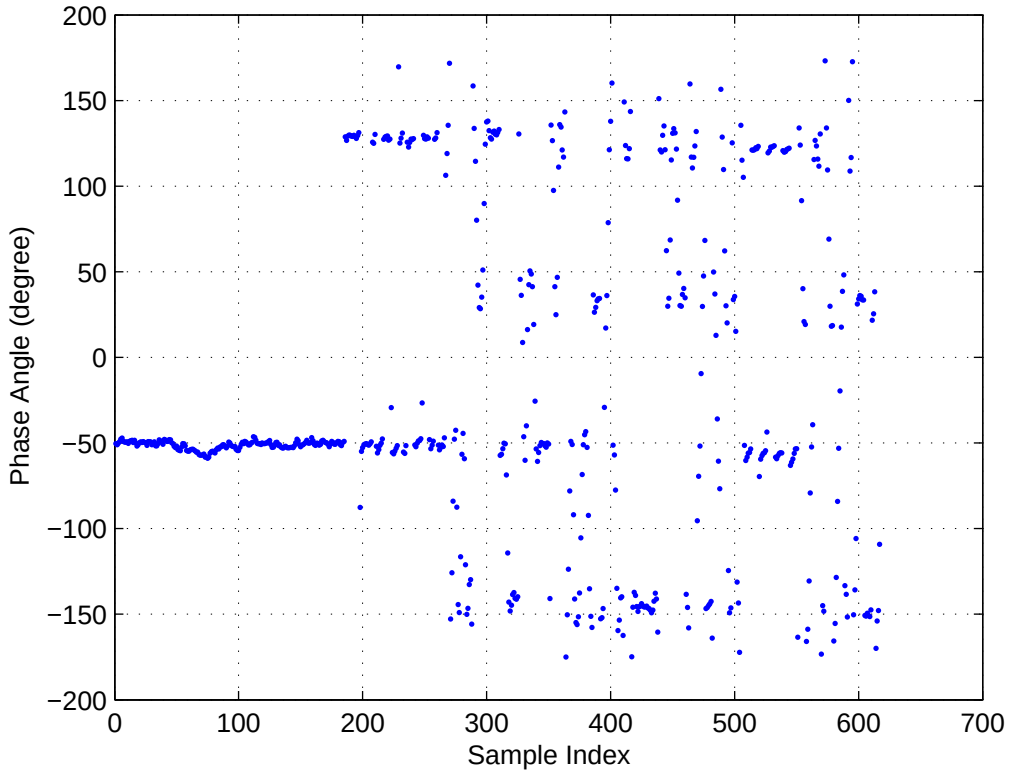

Figure 6.5: Phase angle plot of the burst 2, showing the CW preamble, BPSK unique word, and QPSK data

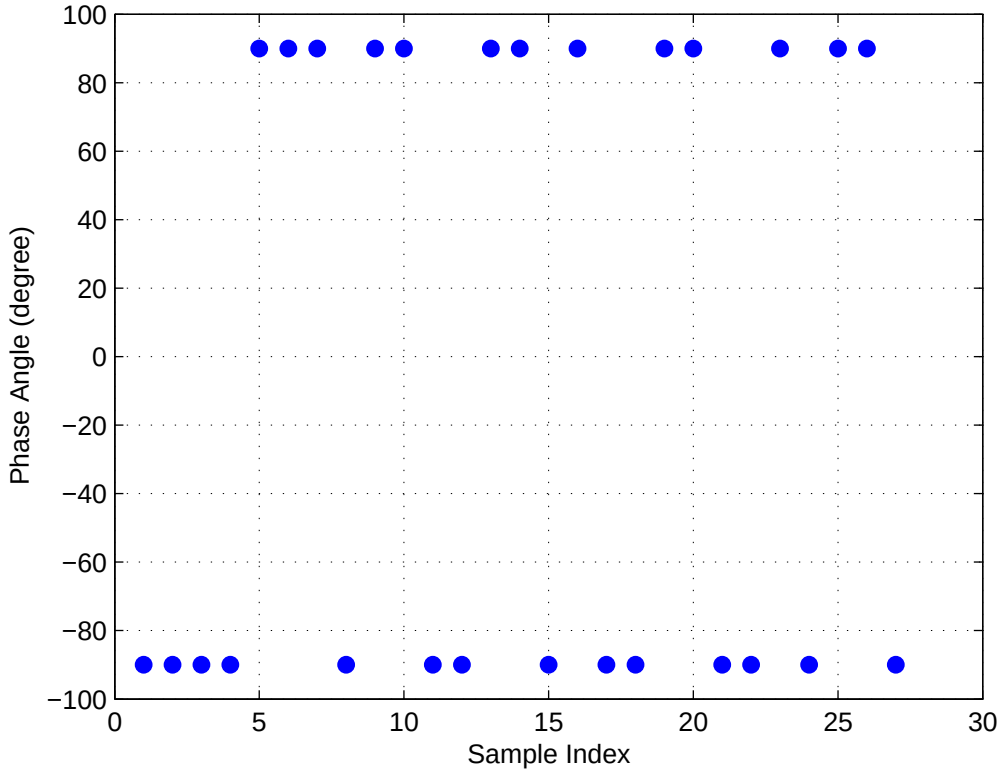

Figure 6.6: Phase angle plot of the unique word

Because the sampling rate is only 78.125 kSPS, it is not possible to determine the actual pulse shape of the transmitted data from the time domain plots. However, by integrating the magnitude of the spectrum of the data in each burst, the pulse shape is seen to be a raised cosine pulse (as expected), as shown in Figure 6.7. Recall that Iridium signals use root raised cosine pulse shaping with 'rolloff factor' of 0.4 [6].

It is assumed that the modulated data of every burst share the same symbol rate of 25 kSy/s. When the symbol period corresponding to 25 kSy/s is used to create an eye diagram of a data burst, the eye is open, as shown in Figure 6.8.

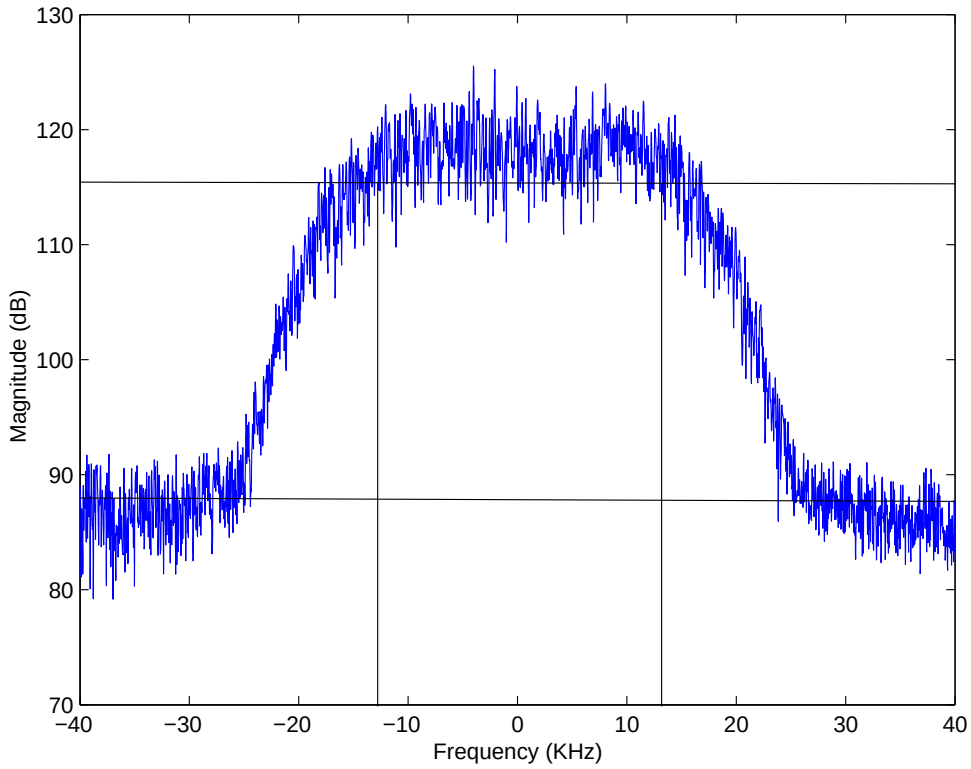

Figure 6.7: Integrated spectra of data bursts, characterizing the individual pulse shape

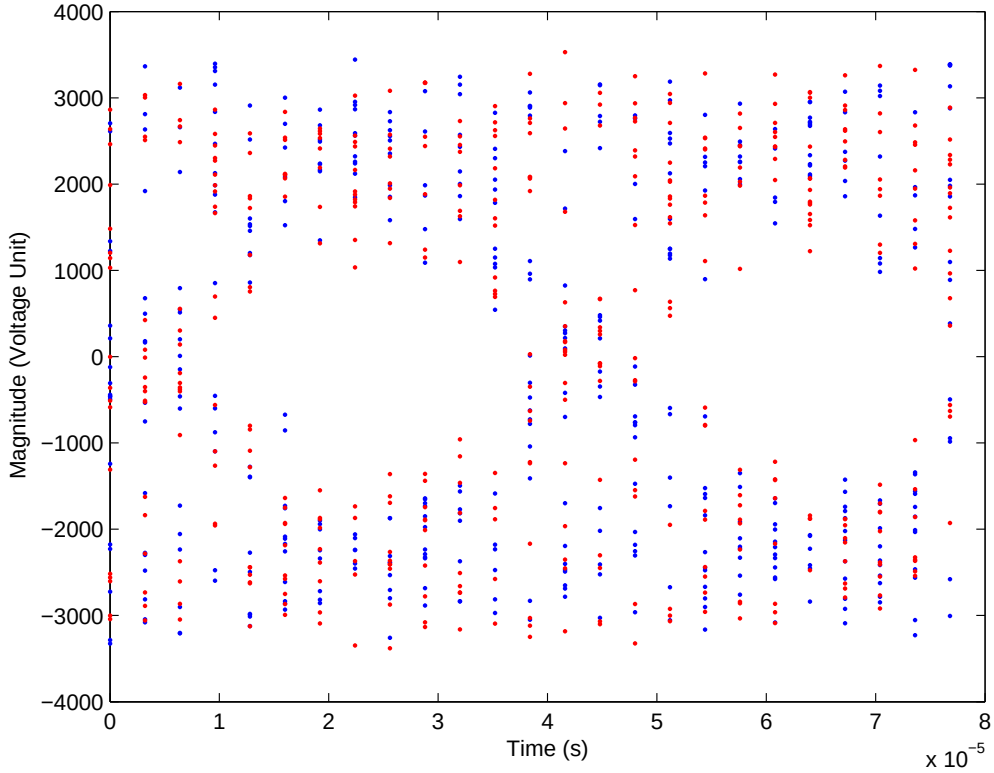

Figure 6.8: Two cycles of eye diagram for burst 1

6.3 Performance Comparison Between Detect/Blank Vs Detect/Cancel

In this section, the proposed algorithm, Detect/Cancel is compared with Detect/Blank method on real data. Time domain blanking to mitigate RFI is discussed in previous chapters. Figure 6.9 shows the integrated spectrum of the original signal, time blanked signal and "synthesized and subtracted" signal generated from real data.

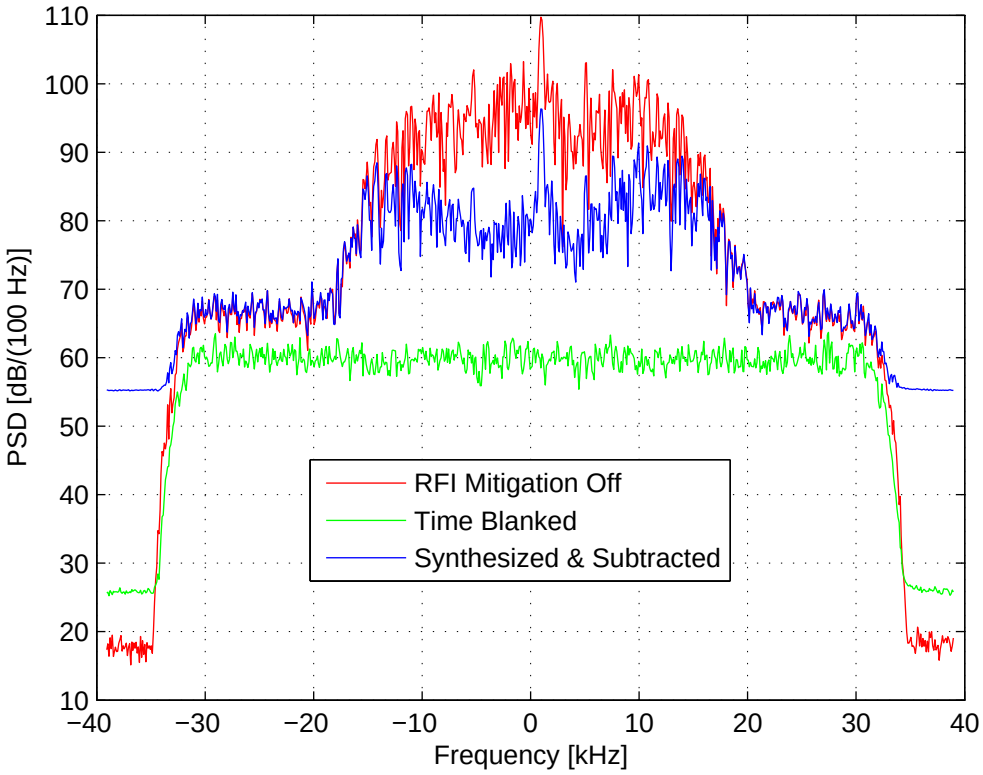

Figure 6.9: Performance comparison between Detect/Blank Vs Detect/Cancel on real data: before and after integrated spectrum

The original Iridium signal is taken from an Argus receiver output. In the detector, the threshold, β is set to 10 dB for all the cases. The portion of the original signal

analyzed here contains a single burst and the signal strength is 41 dB SNR. It is observed that the time blanking achieves 38 dB suppression, while the "synthesized and subtracted" signal achieves 18 dB suppression.

The performance of these two algorithms on real data show similar type of suppression characteristics found in simulation. Like simulation, time blanking outperforms "synthesization and subtraction" method.

The suppression achieved by "estimation and synthesis" process on the real signal is lower than that of simulation. This is quite understandable as the simulated signal contains only additive Gaussian noise; while the real signal contains all the channel effects such as doppler shift, fading, multipath and all the effects due to the limitation of the hardware. also note that a very crude method was implemented during symbol time recovery process. If symbol time τ was estimated as the peak of the triangle in Figure 4.8 instead of the highest total average energy, overall cancelation would have been improved. All these impairment degrades the performance of estimating the symbols and synthesizing the signal which lead towards lower suppression in real data.

Chapter 7

Conclusion

7.1 Research Contributions

The thesis describes a technique to mitigate radio frequency interference (RFI) from Iridium. In this thesis, an algorithm to "detect/cancel" the RFI from Iridium is presented. In this thesis we have achieved the following:

- An algorithm was proposed to mitigate RFI from Iridium. The proposed algorithm was a temporal method in which Iridium signal was detected, estimated, synthesized, and finally subtracted from the telescope input.
- Proposed algorithm was validated using simulated Iridium data. A complete performance of the system was simulated and analyzed for simulated data. It was observed that the proposed interference mitigation scheme achieves 14 dB suppression for 20 dB SNR, and 8 dB suppression for 10 dB SNR, assuming perfect detection. The canceling performance increased with the increase of SNR as with increase of SNR, it is possible to estimate the parameters and demodulate the symbols more accurately.
- Proposed algorithm was validated using real data captured from the Argus

radio telescope to verify the effectiveness of proposed algorithm in a real world scenario. It was observed that the proposed interference mitigation scheme achieves 18 dB suppression for 41 dB SNR, assuming perfect detection.

- A comparative study of the performance of the proposed algorithm for both the simulated data and the real data was conducted. It was observed that the proposed algorithm achieves similar canceling performance, even though it performs slightly better for simulated data; that is because simulated data had only AWGN while real data had few other channel effects which degrades estimation accuracy.

- A comparative study between the performances of the proposed algorithm (detect/cancel) with another well known algorithm (detect/blank) was conducted for both simulated and real data. It was observed that the time blanking scheme, for 41 dB SNR, achieves 38 dB suppression for real data and 29 dB for both simulated data. In both cases, it outperforms the proposed algorithm.

7.2 Future Research

The following work should be considered in future:

- Modify the detector, estimator and canceler to improve the effectiveness. Specifically, improve the symbol timing estimation in Section 4.4.3 by implementing the optimal estimation method described in the same section.

- Use of multirate techniques to reduce computational burden.

- An adaptive sidelobe based canceling algorithm could be implemented to mitigate the RFI from Iridium. In this method, a beamformer will be created with nulls determined from the estimated parameters of the Iridium signal.

Bibliography

[1] L. Wood and P. Worfolk et al. *SaVi - Satellite constellation Visualisation software*. http://savi.sf.net/, 2006.

[2] Timothy Pratt, Charles W. Bostian, and Jeremy Allnutt. *Satellite Communications*. John Wiley & Sons, 2nd edition, 2002.

[3] Jim Cohen, Titus Spoelstra, Roberto Ambrosini, and Wim van Driel, editors. *CRAF Handbook for Radio Astronomy*. Committee on Radio Astronomy Frequencies (CRAF), European Science Foundation, 79-81, third edition, 2005.

[4] Titus Spoelstra, editor. *CRAF Handbook for Frequency Management*. Committee on Radio Astronomy Frequencies (CRAF), European Science Foundation, Strasbourg, France, February 2002.

[5] http://www.iridium.com/.

[6] Donald H. Martin. *Communication Satellites*. The Aerospace Press, 2000.

[7] Patrick Flanagan. *Iridium fallout: Trickle-down effect*, volume 33 of 7. Horizon House Publications, July 1999.

[8] Nikos Drakos and Ross Moore, editors. *The Very Large Array Observational Status Summary*. The National Radio Astronomy Observatory (NRAO), 1999.

[9] *ITU-R Handbook on Radio Astronomy*. ITU-R Radiocommunications Bureau, Geneva, Switzerland, 2003.

[10] Titus Spoelstra, editor. *Update CRAF-Iridium Workplan.* Committee on Radio Astronomy Frequencies (CRAF), European Science Foundation, Strasbourg, France, January 2000.

[11] S.W. Ellingson and G.A. Hampson. Mitigation of radar interference in l-band radio astronomy. *Astrophysical Journal Supplement Series*, 147(1):167–176, July 2003.

[12] A. J. Boonstra, Amir Leshem, A. J. van der Veen, A. Kokkele, and G. Schoonderbeek. The effect of blanking of tdma interference on radio-astronomical observations: experimental results. *Acoustics, Speech, and Signal Processing, 2000. ICASSP '00. Proceedings. 2000 IEEE International Conference on*, 6:3546 – 3549, 2000.

[13] S.W. Ellingson, J. Bunton, and J.F. Bell. Removal of the glonass c/a signal from oh spectral line observations using a parametric modelling technique. In *Astrophysical Journal Supplement*, volume 135, pages 87–93, July 2001.

[14] S.W. Ellingson. Capabilities and limitations of adaptive canceling for microwave radiometry. *IEEE 2002 Intn'l Geoscience and Remote Sensing Symposium (IGARSS 2002), Toronto*, pages 3:1685–7, June 2002.

[15] Various authors. Special section on mitigation of radio frequency interference in radio astronomy. *Radio Sci.*, 40, RS5S01, doi:10.1029/2005RS003268, 2005.

[16] http://iridium.infosat.com/.

[17] John G. Proakis. *Digital Communications.* McGraw-Hill, 2001.

[18] Steven M. Kay. *Fundamentals of Statistical Signal Processing: Detection Theory.* Prentice Hall PTR, 1998.

[19] Steven M. Kay. *Fundamentals of Statistical Signal Processing: Estimation Theory.* Prentice Hall PTR, 1993.

[20] Sanjit K. Mitra. *Digital Signal Processing: A Computer-Based Approach.* McGraw-Hill, 1998.

[21] Martin S. Roden. *Analog and Digital Communication Systems.* Discovery Press, 2001.

[22] Jeffrey H. Reed. *Software Radio: A Modern Approach to Radio Engineering.* Prentice Hall PTR, 2002.

[23] Balaji Srinivasan. *"IS.54 Digital Cellular Modem Implementation on the TMS320C5x": Application Report.* Number SPRA138. Texas Instruments, October 1994.

[24] Leon W. Couch II. *Digital and Analog Communication Systems.* Prentice Hall, 1997.

[25] Theodore S. Rappaport. *Wireless Communications: Principles and Practice.* Prentice Hall PTR, 2001.

[26] S.W. Ellingson and G.A. Hampson. "argus: An l-band array for detection of astronomical transients". *IEEE Int'l Ant. and Prop. Sym.*, pages (3:256–9), Columbus, OH, June 2003.

[27] S.W. Ellingson and P. McDougle. "iridium: Characterization and countermeasures". *Workshop on Mitigation of Radio Frequency Interference in Radio Astronomy (RFI2004)*, Penticton, BC, Canada, July 2004.

[28] Patrick McDougle. "analysis of bursts from iridium satellites analysis of bursts from iridium satellites". March 2004. Unpublished manuscript.

Appendix A

Copyright Permission

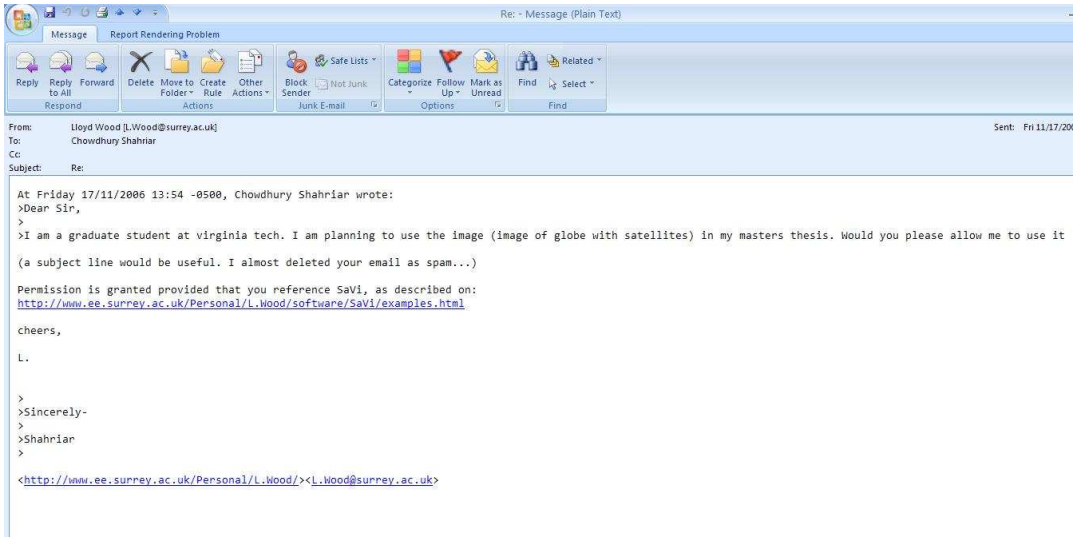

Figure A.1: Email showing the permission of using copyrighted images

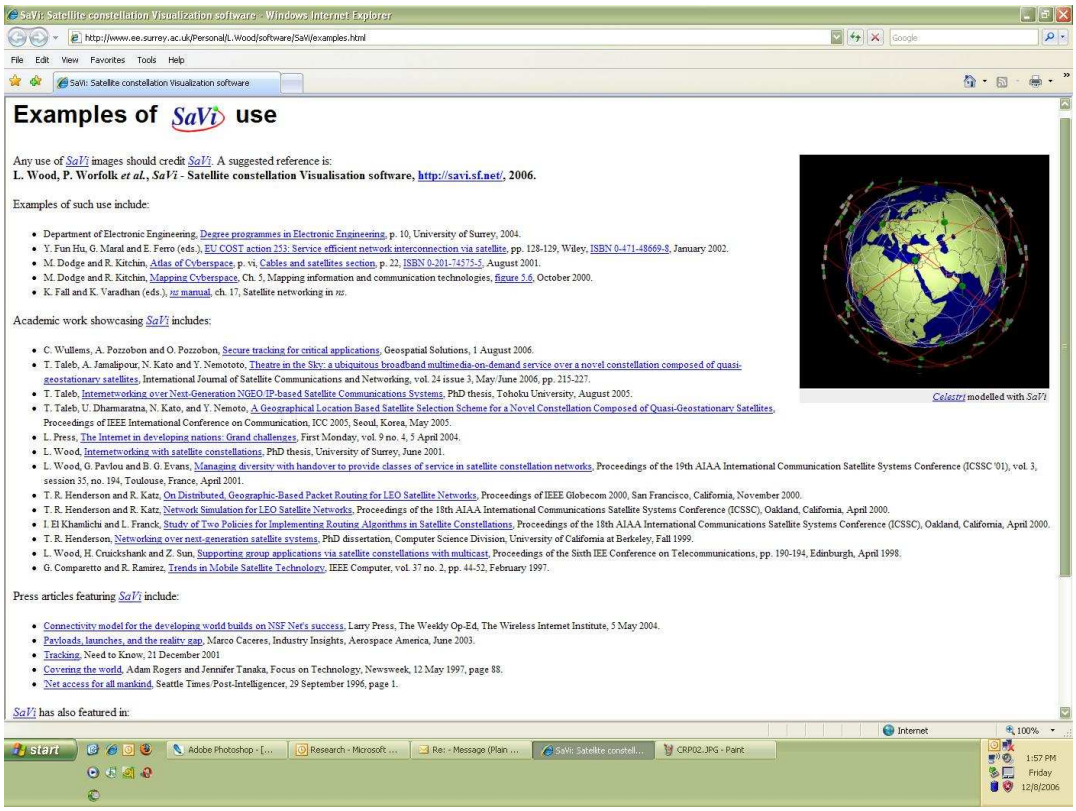

Figure A.2: Web site contains the permission of using copyrighted images

Vita

Chowdhury Shahriar received his B.S. degree in Electrical Engineering from the Bradley Department of Electrical and Computer Engineering at Virginia Polytechnic Institute and State University in the fall of 2002 and subsequently joined the same department to pursue M.S. degree in the spring of 2003.

After spending one year as a graduate student with the department, Shahriar began research with the Mobile and Portable Radio Research Group (MPRG) under the supervision of Dr. Steven Ellingson. His research interests include physical layer system analysis of spread spectrum, UWB and OFDM systems, and applied DSP.